Stimulated Raman scattering in 10 and 100 atmosphere molecular hydrogen
by Michael Jack Runkel

A thesis submitted in partial fulfillment of the requirements for the degree of Master of Science in Physics
Montana State University
© Copyright by Michael Jack Runkel (1989)

Abstract:
This thesis presents a study of Stimulated Raman Scattering in 10 and 100 atmosphere molecular hydrogen using a broadband, multimode, xenon chloride excimer laser operating at ultraviolet wavelengths. Stimulated Raman Scattering was initiated in the medium using optimally aligned pump (308 nm) and Stokes (351 nm) beams. Raman gain data was collected for the cases of well-correlated and uncorrelated pump and Stokes beams. Theory was fit to data via numerical calculation using the multimode, fixed random phase and temporal square pulse models with variable pulse length as fitting parameter. Results of the data fits were compared to the results of previous work, used to compare the 10 and 100 atmosphere cases, and to account for differences between the correlated and uncorrelated results at fixed pressure. Comparison of the pulse times derived from numerical data fitting and from measurements of peak power density showed agreement to within the error bars found in the experiment.

Additional topics intended to supplement the main body of the thesis include a formal development of Riemann's method for the solution of second order hyperbolic partial differential equations, and its application to the Raman equations, and a characterization of molecular hydrogen as a Raman scattering medium using elementary quantum mechanics and spectroscopic theory.

STIMULATED RAMAN SCATTERING IN 10 AND 100 ATMOSPHERE MOLECULAR HYDROGEN

by

Michael Jack Runkel

A thesis submitted in partial fulfillment
of the requirements for the degree

of

Master of Science

in

Physics

MONTANA STATE UNIVERSITY
Bozeman, Montana

December 1989

N378
R867

APPROVAL

of a thesis submitted by

Michael Jack Runkel

This thesis has been read by each member of the thesis committee and has been found to be satisfactory regarding content, English usage, format, citations, bibliographic style, and consistency, and is ready for submission to the College of Graduate Studies.

11-27-89
Date

John L. Carlson
Chairperson, Graduate Committee

Approved for the Major Department

11-27-89
Date

Robert J. Swenson
Head, Major Department

Approved for the College of Graduate Studies

12/18/89
Date

Henry L. Parsons
Graduate Dean

STATEMENT OF PERMISSION TO USE

In presenting this thesis in partial fulfillment of the requirements for a master's degree at Montana State University, I agree that the Library shall make it available to borrowers under rules of the Library. Brief quotations from this thesis are allowable without special permission, provided that accurate acknowledgment of source is made.

Permission for extensive quotation from or reproduction of this thesis may be granted by my major professor, or in his absence, by the Dean of Libraries when, in the opinion of either, the proposed use of the material is for scholarly purposes. Any copying or use of the material in this thesis for financial gain shall not be allowed without my written permission.

Signature Michael Rumkel

Date November 27, 1989

ACKNOWLEDGEMENTS

I would like to thank my advisor, John Carlsten, for the opportunity to work on this project. He allowed me the freedom to pursue ideas on my own and consequently to take this project in any reasonable direction. As a result I have gained an education and experience of scope and depth which would not have been possible otherwise. The other members of this research group have also provided invaluable assistance. David MacPherson and Rand Swanson gave help on many sticking points during this work. Their assistance has been invaluable. Thanks are also due to Scott Remington for his help in collecting experimental data, which saved me a number of miles in running around the optical table, and for his expertise in computing. I am indebted to Phil Battle for frank and honest questions and concerns during the course of the numerical work and data fitting, and for pointing out many things that I had missed.

It is a rare opportunity for any student to have interacted with a teacher as eloquent as Dr. R. T. Robiscoe. I would like to express my gratitude for his lectures on mathematical physics, including hyperbolic partial differential equations, and Bessel functions which served me well in my research on Riemanns method and the solution of the Raman equations.

Thanks also to my other committee members, J. E. Drumheller, and G. Tuthill, for the time they took in reading my thesis and the revisions they suggested.

I would also like to express my appreciation to the secretaries of the Physics Department. Their help has been a great aid to the successful completion of this thesis.

I would never have brought this thesis to a successful conclusion if not for my wife Terry. She provided me with invaluable support and kept a level head when I had lost mine, and always saw to it that I did the right thing.

Finally, I would like to thank my parents for allowing me the freedom to pursue my goals, and for their continual interest in and support of my progress throughout my academic career.

TABLE OF CONTENTS

Page

APPROVAL ii

STATEMENT OF PERMISSION TO USE iii

ACKNOWLEDGMENTS iv

TABLE OF CONTENTS v

LIST OF TABLES vii

LIST OF FIGURES viii

ABSTRACT x

1. INTRODUCTION 1

2. ANALYTIC SOLUTIONS OF THE RAMAN EQUATIONS 6

   Introduction 6
   Theory 6

3. APPARATUS 13

   Introduction 13
   Data Acquisition and Reduction 16

4. LINEWIDTH MEASUREMENTS 19

   Introduction 19
   The Fabry-Perot Interferometer 19
   Plate Separation Method 26

5. NUMERICAL ANALYSIS 29

   Introduction 29
   Modeling the Broadband Laser 30
   The Riemann Integral 34
   Program Testing 37
   Data Fitting 40

TABLE OF CONTENTS - Continued

Page

6. ANAYLSIS, INTERPRETATION, AND CONCLUSION 45

Introduction 45
Experimental Data Characterization 46
Comparison to Previous Work 47
Comparison of 10 and 100 Atmosphere Results 48
Comparison of Correlated and Uncorrelated Results 49
Comments on the Temporal Square Pulse Model 50

REFERENCES CITED 52

APPENDICES 56

Appendix A - Riemann's Method 57
Appendix B - Computer Programs 63

GLATT 64
LFELD 66
RAMAN 71
AVEFIL 75
DEVIATION 78

Appendix C - Characterization of Molecular Hydrogen as a Raman Scattering Medium 81

Vibrational Spectra 83
Rotational Spectra 86
Summary 90

LIST OF TABLES

Table Page

1. Pulse times derived from numerical fits to data.....46

LIST OF FIGURES

Figure		Page
1.	Three level energy diagram representing the Raman scattering process	7
2.	Contour used in the solution of the Raman equations via Riemanns method	11
3.	Schematic of experimental apparatus	14
4.	Typical optical delay data showing the effect of smoothing	17
5.	Theoretical output of an idealized Fabry-Perot	20
6.	Typical digitized output of the Fabry-Perot operating in Fizeau mode	24
7.	Schematic of apparatus used in measurement of the plate spacing	25
8.	Fabry-Perot rotation angle as a function of order number	28
9.	Typical electric field produced by the program LFELD	32
10.	Typical temporal profile of the XeCl laser output	33
11.	Numerical gain curve showing transient behavior	38
12.	Numerical gain curves fit to 100 atm uncorrelated data	41
13.	Numerical gain curve fit to 10 atm uncorrelated data	42
14.	Numerical gain curves fit to 100 atm correlated data	43
15.	Numerical gain curve fit to 10 atm correlated data	44
16.	Contour used in developing generalized Riemann solution of hyperbolic partial differential equations	59
17.	Contour used to adapt generalized Riemann solution to the Raman equations	62

LIST OF FIGURES - Continued

Figure Page

18. Computer program GLATT 64

19. Computer program LFELD 66

20. Computer program RAMAN 71

21. Computer program AVEFIL 75

22. Computer program DEVIATION 78

23. Geometry used in determining the polarizability $\alpha_{z'z'}$ for Rotational Raman Scattering 88

ABSTRACT

This thesis presents a study of Stimulated Raman Scattering in 10 and 100 atmosphere molecular hydrogen using a broadband, multimode, xenon chloride excimer laser operating at ultraviolet wavelengths. Stimulated Raman Scattering was initiated in the medium using optimally aligned pump (308 nm) and Stokes (351 nm) beams. Raman gain data was collected for the cases of well-correlated and uncorrelated pump and Stokes beams. Theory was fit to data via numerical calculation using the multimode, fixed random phase and temporal square pulse models with variable pulse length as fitting parameter. Results of the data fits were compared to the results of previous work, used to compare the 10 and 100 atmosphere cases, and to account for differences between the correlated and uncorrelated results at fixed pressure. Comparison of the pulse times derived from numerical data fitting and from measurements of peak power density showed agreement to within the error bars found in the experiment.

Additional topics intended to supplement the main body of the thesis include a formal development of Riemann's method for the solution of second order hyperbolic partial differential equations, and its application to the Raman equations, and a characterization of molecular hydrogen as a Raman scattering medium using elementary quantum mechanics and spectroscopic theory.

CHAPTER ONE

INTRODUCTION

Raman scattering is a process whereby light, typically from a laser, interacts with a scattering medium, causing a frequency shifted photon to be emitted. As such, it is a three level process. The incident, or pump, photon drives the atom into a superposition of electronic states. The transition from the superposition state to a third state (a vibrational or rotational state of the lower electronic state) causes a photon, frequency shifted from the incident light, to be emitted. For a frequency downshift, the emission is known as Stokes radiation. Conversely, if the emission is higher in frequency it is known as Anti-stokes emission. Raman scattering was first observed by C. V. Raman[19] in 1928.

Raman scattering can be viewed in at least two ways. The first treats the process in terms of small ensembles of atoms from the viewpoint of scattering theory[20], complete with derivatons of appropriate cross sections[21]. The second viewpoint concentrates on the derivation and solution of the "equations of motion" for the pump and Stokes electric fields propagating through large (macroscopic) mediums, and the coherence Q of the medium (i.e. the response of the medium to excitation). Of interest in this picture are the growth of the Stokes field (i.e. the gain), the depletion of the pump field, and the response of the medium to the fields. Numerous approaches have been used to obtain the equations of motion for the process. Historically, the equations have been derived semi-classically using Maxwell's wave equations for the fields with the nonlinear (induced) polarization of the medium acting as the driving term. It, in turn, is calculated from molecular susceptibilities. Earlier works[1,2,22,23,24] used the Placzek model[25] of molecular

polarizability to obtain this term while later models[3,26] used the quantum mechanical susceptibility. Shen and Bloembergen[22], and Wang[1] derive the Raman equations using Lagrangian densities and Euler's equations. Raymer, Mostowski, and Carlsten[3] employ the Bloch vector formalism and quantum mechanical susceptibilities in deriving the equations, while Raymer and Mostowski[4] use a complete quantum (operator) description for the medium and Stokes fields, but treat the pump classically. Typically the Slowly Varying Envelope Approximation[27] and the Rotating Wave Approximation[27] are relied upon in all methods of derivation of the Raman equations.

The solution of the Raman equations was first presented in full form by Wang[1] using Riemann's method.[13,14,15] Later, Raymer and Mostowski[4] applied Laplace transform methods to obtain the solutions.

The pump sources used in Raman scattering fall into two categories: monochromatic (or nearly so) and broadband. Analysis of the Stokes field solution for monochromatic sources[3] is rather straightforward and serves as a benchmark to which all other models are compared. For the broadband case, there exist numerous models to describe the scattering process. Among these is one known as the "multimode fixed random phase" model[5,26,28]. In this model, it is assumed that an ensemble of atoms emits into a distribution of frequency modes which have constant amplitude and are weighted by a Lorentzian frequency distribution, which is caused by laser linewidth broadening mechanisms. Associated with the individual electric field of each mode is a random phase angle ϕ_n which accounts for the randomness of emission process of the excimer laser. The pump field is then taken to be the sum of a large number of the individual electric fields. The describing equation is $E = \sum_{n=-\infty}^{\infty} A_n \exp[-i(n\delta t + \phi_n)]$. Here δ represents the mode spacing of the laser.

When the pump intensity is very low, only spontaneous Raman scattering takes place. Initiation of the scattering process is due to quantum noise fluctuations[31]. If the

pump intensity is large enough, then the scattering process becomes stimulated or driven by the pump fields. For this case, Raman scattering can be divided into two categories. The first is Raman generation in which only the pump beam enters the medium and causes excitation. The second is Raman amplification in which both a pump beam and a Stokes probe are incident on the medium.

Theory[28] predicts that for generation, the Stokes intensity is independent of the number of modes, and that the pump and Stokes fields are highly (but not necessarily totally) correlated in phase. For amplification, however, the pump and Stokes fields become correlated in phase only at high gain values[3], i.e., high input pump fields or long cell length. A further result is that the broadband gain falls below the monochromatic value at low pump energies or for short cells. Experimentally, the phase correlation issue has been explored by a number of authors[29,30] who have verified the theoretical predictions.

This thesis is the continuation of research begun by Rifkin[5,26]. It attempts to answer questions left behind from that work. Rifkin compared the predictions of the multimode fixed random phase model to experimental data for Raman scattering in molecular hydrogen at 100 and 10 atmospheres pressure. His results at 100 atm pressure matched the data quite well; however, fitting the data at 10 atm was not successful. Two factors attributed to the lack of fit at 10 atm include changing overlap in the pump and Stokes seed alignment in the experimental apparatus, and fluctuations in the laser linewidth between the times when 100 and 10 atm data were taken.

It is the goal of this thesis to investigate stimulated Raman scattering in 10 atm hydrogen and address the questions unanswered by Rifkin. This thesis will describe how the optical alignment was improved to give more stable measurements, as well as how the laser linewidth was monitored using a Fabry-Perot interferometer, which was unavailable at the time of Rifkin's work. Also described will be the numerical techniques used

to fit the data to the one parameter temporal square pulse model. As program testing and numerical calculations progressed, it became apparent that copious amounts of computing power would be necessary to properly address the issue of data fitting. At the time of Rifkin's work, such computing power was not readily available to him, making a protracted numerical analysis untractable, or impractical at best. To conclude the thesis a chapter will be given summarizing and interpreting the results of this project.

This thesis was assembled with the intent that the reader could gain the most important information with the first reading. Topics of secondary importance have been put into appendices for more detailed study later.

Chapter 2 presents the solution of the coupled Raman equations using Riemann's method. It is largely mathematical in content and omission of this chapter in first reading would not interrupt the continuity of the thesis. The most important results of this chapter are equations (2.1) and (2.25); the coupled differential Raman equations, and the integral solution for the Stokes field respectively.

Chapter 3 describes the experimental set-up, data collection and reduction techniques, and deals with experimental error bars as well.

Chapter 4 deals mainly with the role of the Fabry-Perot interferometer in this work. It discusses the basic concepts and jargon of Fabry-Perot interferometry and details how the instrument was used to monitor the lasers linewidth in real time. Included in this chapter is a description of a highly accurate optical method for determination of the Fabry-Perot plate spacing.

Chapter 5 is the core of this thesis. In this chapter is a discussion on the numerical methods used to generate the broadband laser field, and to evaluate the Stokes field solution derived in Chapter 2. The mathematical background is provided as well as a brief description of the computer codes involved. Further, Chapter 5 discusses the methods by which the computer codes were applied to fit the experimental data.

Chapter 6 discusses the results of this work. Here, the numerical results will be used to account for the features of the experimental data. The data fits will be given in terms of scaling arguments and pulse lengths derived from the numerical model found in Chapter 5. The results will also be compared to previous work, and concluding remarks regarding the one parameter temporal square pulse model in stimulated Raman scattering will be made.

Appendix A develops Riemann's method for solving linear second order hyperbolic partial differential equations. Riemann's method is a powerful, although somewhat delicate, tool which seems to have been lost to obscurity, likely superseded by more robust methods such as Laplace transformations.

Appendix B contains the Fortran source codes used in data analysis and numeric fitting.

Appendix C characterizes molecular hydrogen as a Raman scattering medium. Elementary specroscopic models are called upon to determine the types of allowable Raman scattering (i.e. electronic, vibrational, or rotational Raman scattering), and it is shown that the Raman scattering seen in this experiment is mainly vibrational in nature.

CHAPTER TWO

ANALYTIC SOLUTIONS OF THE RAMAN EQUATIONS

Introduction

In this chapter the analytic solution to the transient Raman equations is derived using Riemann's Method (see Appendix A). The solution is presented in this thesis for a number of reasons. First, the emphasis in the literature appears to be in the derivation of the Raman equations, with the solution merely being quoted. Secondly, the solutions for E_s and Q^* presented by Wang[1] are in notation which is non-transparent. For these reasons, it seems appropriate to include the full derivation of the integral solution for the Stokes field $E_s(z,\tau)$. It should be noted that Riemann's Method is not the only way to solve the Raman equations. They are susceptible to solution using Laplace transforms as well[4]. The solution readily lends itself to numeric evaluation as will be discussed in Chapter 5.

Theory

In solving the Raman equations, the procedure of Carman et. al.[2] will be followed, but the equations shall be written in a more standard notation. The Raman equations are[3]

$$\frac{\partial Q^*}{\partial t} + \Gamma Q^* = i\kappa_1 E_S E_L^* \qquad (2.1a)$$

and

$$\frac{\partial E_S}{\partial z} = -i\kappa_2 Q^* E_L \qquad (2.1b)$$

Q^* denotes the coherence of the medium, Γ is the Raman linewidth of the medium, E_S and E_L refer to the Stokes and pump (laser) fields respectively, and κ_1 and κ_2 are the coupling constants having the form given by Raymer et. al.[3] of

$$\kappa_1 = \frac{d_{12}d_{23}}{2\hbar^2\Delta_L} \tag{2.2a}$$

and

$$\kappa_2 = \frac{\pi N \omega_S v_S d_{12} d_{23}}{c^2 \hbar \Delta_L} \tag{2.2b}$$

Here d_{ij} refers to the dipole matrix element between states i and j, v_s is the velocity of propagation in the medium, and Δ_L is the detuning from the $|1\rangle \rightarrow |2\rangle$ transition.

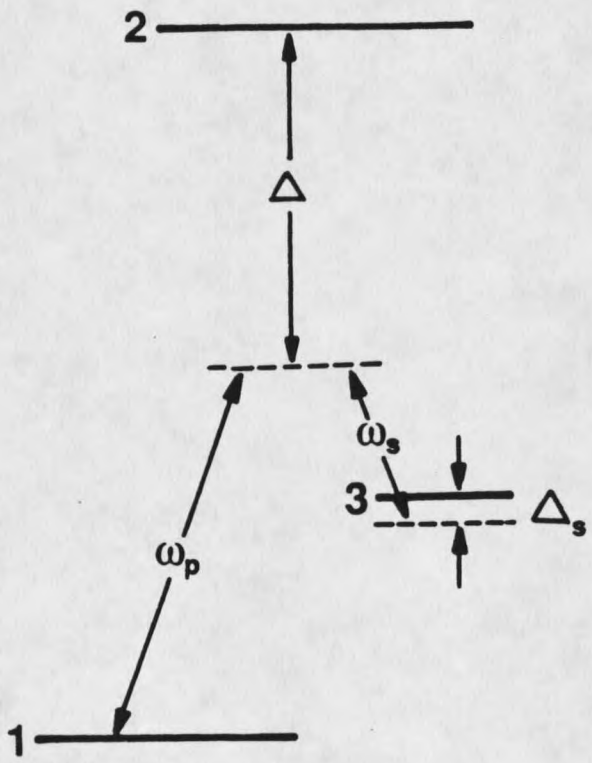


Figure 1. Three level energy diagram representing the Raman scattering process. ω_p and ω_s denote the pump and Stokes frequencies and Δ_L and Δ, the detunings from resonance. |1> and |2> are electronic levels, while |3> denotes a vibrational level of the state |1> which is typically the electronic ground state.

The variables t and z refer to a reference frame which is comoving with the pulse. They are connected to the laboratory frame by the relations $t = t' - z/v_S$ and $z = z' - v_{pho}t$ and it is assumed that $v_{pho} \ll c$ where v_{pho} refers to the phonon velocity in the medium. Also, the assumption is made that the group velocities of the pump and Stokes are matched and that no pump depletion or medium saturation occurs during the scattering process. Consequently, the laser field may be written as $E_L = E_L(t)$. The Raman equations (2.1) may be decoupled in the classical manner as follows. Rewrite (2.1b) as

$$Q^* = \frac{i}{\kappa_2 E_L}\frac{\partial E_S}{\partial z} \tag{2.3}$$

and take its time derivative to get

$$\frac{\partial Q^*}{\partial t} = \frac{i}{\kappa_2}\left(-\frac{1}{E_L^2}\frac{\partial E_L}{\partial t}\right)\frac{\partial E_L}{\partial z} + \frac{i}{\kappa_2 E_L}\frac{\partial^2 E_S}{\partial z \partial t} \tag{2.4}$$

Substitution of (2.3) and (2.4) into (2.1b) eliminates all Q^* dependence. The result is

$$\left(-\frac{1}{E_L^2}\frac{\partial E_L}{\partial t}\frac{\partial E_S}{\partial z} + \frac{1}{E_L}\frac{\partial^2 E_S}{\partial t \partial z}\right) + \Gamma\frac{\partial E_S}{E_L \partial z} = \kappa_1\kappa_2 \mid E_L \mid^2 E_S \tag{2.5}$$

Using $E_L = E_L(t)$ equation (2.5) can be written as

$$\frac{\partial^2}{\partial z \partial t}\left(\frac{E_S}{E_L}\right) + \Gamma\frac{\partial}{\partial z}\left(\frac{E_S}{E_L}\right) - \kappa_1\kappa_2 \mid E_L \mid^2 \left(\frac{E_S}{E_L}\right) = 0 \tag{2.6}$$

If the same procedure is applied to (2.1) to eliminate the E_S dependence, the decoupled Q^* equation is

$$\frac{\partial^2 Q^*}{\partial z \partial t} + \Gamma\frac{\partial Q^*}{\partial z} - \kappa_1\kappa_2 \mid E_L \mid^2 Q^* = 0 \tag{2.7}$$

Letting $F = Q^*$ or E_S/E_L equations (2.6) and (2.7) take the form

$$\frac{\partial^2 F}{\partial z \partial t} + \Gamma\frac{\partial F}{\partial z} - \kappa_1\kappa_2 \mid E_L \mid^2 F = 0 \tag{2.8}$$

The first derivative in z can be eliminated through the transformation $F(z,t) = U(z,t)e^{-\Gamma t}$. Calculating derivatives shows that

$$\frac{\partial F}{\partial z} = U_z e^{-\Gamma t} \tag{2.9a}$$

and

$$\frac{\partial^2 F}{\partial z \partial t} = e^{-\Gamma t}(U_{zt} - \Gamma U_z) \tag{2.9b}$$

with the subscripts denoting partial derivatives. Substitution gives the equation

$$U_{zt} - \kappa_1 \kappa_2 \mid E_L(t) \mid^2 U = 0 \tag{2.10}$$

Equation (2.10) can be simplified further if the change of variables

$$p(t) = \int_{-\infty}^{t} \mid E_L(\xi) \mid^2 d\xi \tag{2.11}$$

is applied. It should be noted that p is proportional to the energy in the laser pulse up to the time t. Again, calculation of appropriate derivatives shows

$$U_t = U_p \mid E_L \mid^2 \tag{2.12a}$$

and

$$U_{tz} = U_{pz} \mid E_L \mid^2 \tag{2.12b}$$

Equation (2.10) becomes

$$\frac{\partial^2 U}{\partial p \partial z} - \kappa_1 \kappa_2 U = 0 \tag{2.13}$$

This is (2.8) transformed to normal form. The variables p and z are the normal coordinates. The initial conditions of interest given by Carmen et. al.[2] are

$$\partial E_S / \partial z = Q^*(z) = 0 \tag{2.14a}$$

at $t = -\infty$, and

$$E_S(t,0) = E_0 \tag{2.14b}$$

The first equation above is the condition that there is no excitation in the medium before the laser pulse arrives. The second is just the input Stokes field at the entrance of the Raman cell. Translated into the notation of (2.13) they become

$$\frac{\partial U}{\partial z} = 0, \text{ and } U(p,0) = U_0 \tag{2.15}$$

Riemann's Method can now be applied to (2.13). The first step is to find the Riemann function v for the problem. Since $a(p,z) = b(p,z) = f(p,z) = 0$ in (2.13), the associated Riemann function equation is

$$v_{pz} - \kappa v = 0 \tag{2.16}$$

Here, $\kappa = \kappa_1\kappa_2$. To solve (2.16) let $v(p,z;\alpha,\beta) = F(s)$ where $s = (p-\alpha)(z-\beta)$. This transformation will change (2.16) into an ordinary differential equation. Repeated application of the chain rule allows (2.16) to be written as

$$sF_{ss} + F_s - \kappa F = 0 \tag{2.17}$$

Define a new variable λ via $\lambda = \sqrt{4ks}$ and transform, again using the chain rule repeatedly, to obtain the Modified Bessel equation of order zero

$$F_{\lambda\lambda} + \frac{1}{\lambda}F_\lambda - F = 0 \tag{2.18}$$

The solution to (2.18) is

$$v(p,z;\alpha,\beta) = I_0[\sqrt{4\kappa(p-\alpha)(z-\beta)}] \tag{2.19}$$

Explicit calculation shows that v fulfills the conditions (given in equation (A.9) of Appendix A) placed on Riemann-Green functions.

To complete the solution it remains to evaluate equation (A.15) of Appendix A. In p and z notation it reads

$$u\Big|_{P=(p,z)} = uv\Big|_{R=(p,0)} - \int_0^p u\frac{\partial v}{\partial p'}dp' + \int_0^z v\frac{\partial u}{\partial z'}dz' \tag{2.20}$$

The integration contour is shown in Figure 2.

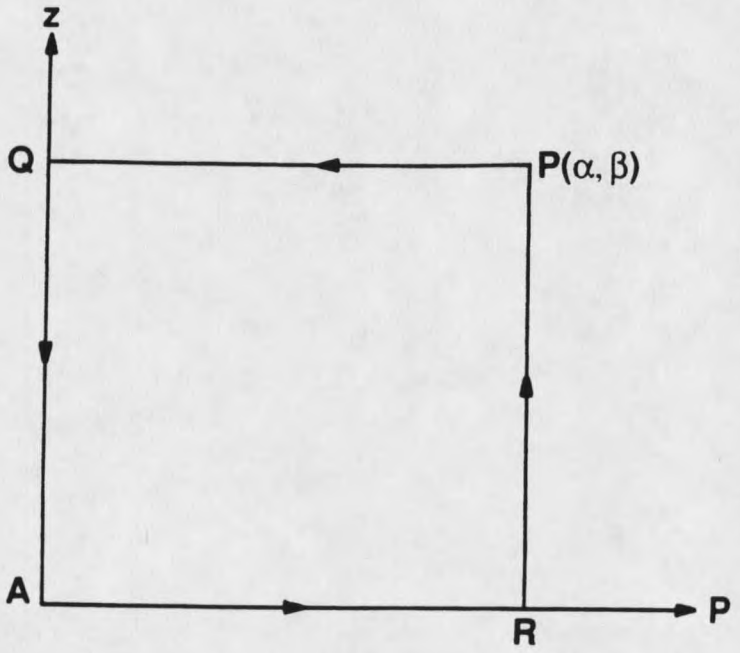


Figure 2. Contour used in the solution of the Raman equations via Riemann's method. The boundary conditions are stipulated along the p and z axes.

The second integral vanishes due to the initial condition (2.15). The first integral is evaluated as follows

$$\int_0^p uv_p dp' = \int_p^0 u(p',0)\frac{\partial}{\partial p'}I_0\sqrt{4\kappa z(p-p')}\,dp' \tag{2.21}$$

Here $\beta = 0$ as shown in Figure 2. Calculating the derivative of the Bessel function gives the result

$$\int_0^p u v_p dp' = -\int_0^p u(p',0)\left(\frac{\kappa z}{p-p'}\right)^{1/2} I_1\sqrt{4\kappa z(p-p')}\,dp' \tag{2.22}$$

Now, transform back to original variables using $dp = |E_L(t)|^2 dt$ and $E_S(t)/E_L(t) = U\exp(-\Gamma t)$ and appropriate dummy indicies. The complete result is

$$E_S(z,t) = E_S(0,t) + \sqrt{\kappa_1\kappa_2 z}\,E_L(t)\int_{-\infty}^{t} e^{-\Gamma(t-t')}E_L^*(t')E_S(0,t')\frac{I_1[\sqrt{4\kappa_1\kappa_2 z(p(t)-p(t'))}]}{\sqrt{p(t)-p(t')}}dt' \tag{2.23}$$

By similar methods it can be shown that the coherence may be written as

$$Q^* = i\kappa_1\int_{-\infty}^{t} e^{-\Gamma(t-t')}E_L^*(t')E_S(0,t')I_1[\sqrt{4\kappa_1\kappa_2 z(p(t)-p(t'))}]dt' \tag{2.24}$$

To be consistent with notation used by Raymer et. al.[3] let $t \rightarrow \tau$ and change limits from $-\infty$ and t to 0 and τ. For the dummy variable τ' the Stokes field solution reads

$$E_S(z,\tau) = E_S(0,\tau) + \sqrt{\kappa_1\kappa_2 z}\,E_L(\tau)\int_0^{\tau}\frac{E_L^*(\tau')E_S(0,\tau')}{\sqrt{p(\tau)-p(\tau')}}e^{-\Gamma(\tau-\tau')}I_1[\sqrt{4\kappa_1\kappa_2(p(\tau)-p(\tau'))}]d\tau' \tag{2.25}$$

CHAPTER THREE

APPARATUS

Introduction

It is the goal of this work to investigate the theory of stimulated Raman scattering with broadband lasers. In principle, the experiment should be designed and executed with the versatility to probe as many of the theoretical predictions as possible. In practice, however, this usually proves to be impractical for various reasons and the experiment may need to be restricted in scope. To that end, this experiment was designed to examine the Raman gain as a function of the correlation between temporal envelopes of the pump and Stokes beams, their respective energies and response to changes in the medium. This was achieved in the following manner.

The laser light used in this experiment was produced by an injection locked Lambda Physik EMG 150 ET pulsed, gas discharge excimer laser using xenon chloride as the lasing medium. This laser and its broadband characteristics are well described by Rifkin[5] and will not be discussed in this thesis, save for a brief description given in Chapter 5. The laser was tuned to operate on the 308.15 nm spectral line of the XeCl, i.e. in the ultraviolet. The pulses produced had a characteristic temporal length of 13.5 ns and energy of 150 mJ typically. Hence, the average power output per pulse was on the order of ten Megawatts.

For use in the experiment, the beam was made diffraction limited by clipping it with

a circular aperature 4.5 mm in diameter, and reduced in energy as needed along the beam path through the use of appropriate dielectric attenuators.

As shown in Figure 3, the beam was divided into two parts by a beam splitter.

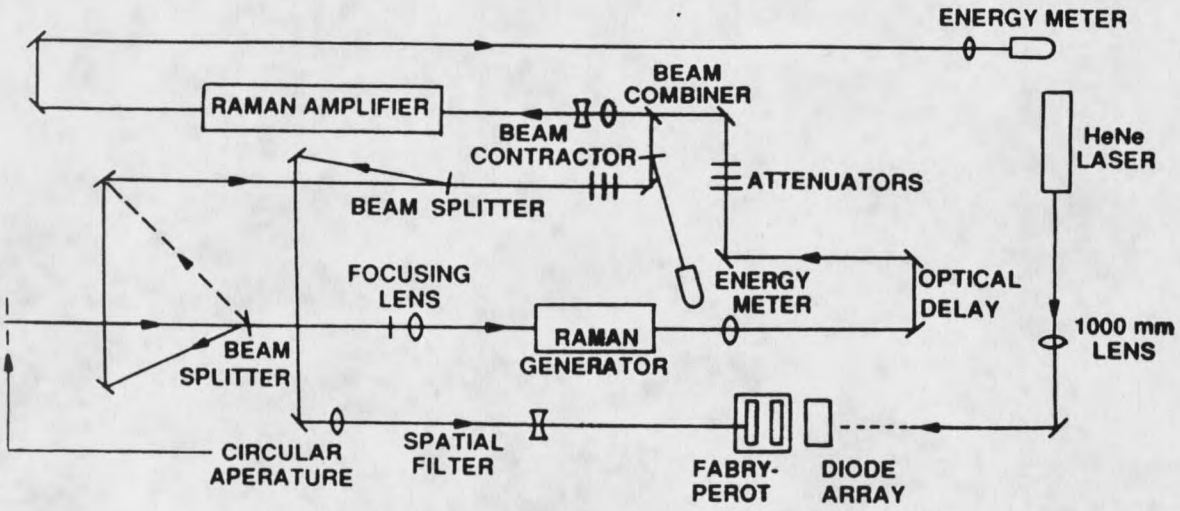


Figure 3. Schematic of experimental apparatus. The dashed line in the UV beam denotes the optical path before modification to improve beam alignment. The dashed HeNe beam indicates usage only for plate spacing measurements.

The transmitted portion was brought to focus at the center of the 50 cm Raman generator cell by a 1 m lens. Before entering this cell, the light was appropriately attenuated to prevent the generation of higher order Stokes processes. Upon exit from this cell, the frequency shifted Stokes light was collimated by another lens. A 100 cm lens was used at 100 atm pressure and a 75 cm lens at 10 atm. These lenses kept the spatial profiles of the Stokes beam comparable in the amplifier cell when the pressure in the cells was changed from one experiment to the next. Next, the Stokes beam passed through the optical delay. The delay consisted of a 3 mirror corner cube mounted on a linear motor drive. With this arrangement, it was possible to make changes of 80 mm (270 ps) in the

optical path length of the Stokes leg. As such, the delay acted as a correlation control device between the pump and Stokes beams. Theory[3,28] predicts that the spontaneously generated Stokes light will become correlated with the pump beam for high gain, which occurs in the generator cell. Hence, if the pump and Stokes legs have the same optical path length, then the two beams should be highly correlated when they reach the amplifier. Once past the delay, the Stokes beam was suitably attenuated and brought to the beam combiner.

The remaining beam, known as the pump beam, travelled a path length comparable to that for the Stokes (within the range provided by the optical delay) and when attenuated as desired was placed directly on the Stokes beam at the beam combiner. The beams were then sent into a beam contracter composed of the 500 and -250 mm lens combination whereupon they passed into the 100 cm Raman amplifier cell. After passing through the amplifier the residual 308 nm wavelength was filtered out and the Stokes energy measured (as a function of delay).

The Raman medium of choice was molecular hydrogen (H_2) and was used in both the generator and amplifier. Molecular hydrogen is a well understood Raman scattering medium and is characterized in Appendix C. The experiment was done twice: initially at 100 atm pressure, and then at 10 atm pressure. These pressure changes served not only to change the Raman linewidth of the medium, but the value of the coupling constant κ_2 in the Raman equations (see Chapter 2). In essence, the experimental apparatus was the same as that used by Rifkin[5] in prior work, however, modifications to the pump leg were made to improve the sensitivity. Initially, Rifkin's work at 100 atm was repeated for verification purposes, but when reduced, the gain enhancement data showed unacceptable scatter. While this was attributed to lack of familiarity with the experimental technique, it also prompted an investigation into making the experimental method more reliable. The problem was due to the so-called "pointing average"; the random movement of the

beam in the plane perpendicular to the direction of propagation about some average beam path. The effect is common in pulsed lasers and results from the statistical nature of the gas discharge process, causing the light to be emitted from the laser cavity at small angles (relative to the average beam path). This effect is magnified by long optical "lever arms" due to the long path lengths involved in this experiment.

Investigation revealed that the pump and Stokes beams jumped in phase (i.e. the same direction and distance) vertically but, were 180 degreees out of phase horizontally, meaning that they jumped in opposite directions from pulse to pulse. Consequently, if the beams were not optimally aligned, then the pump beam would not be completely seeded by the Stokes for optimal stimulation and the resulting data would not only be reduced in peak intensity but, would have considerably more noise.

This problem was solved by placing another mirror in the pump beam (see Figure 3) producing a corner cube in the horizontal. As a result of this modification, the two beams jumped in phase everywhere in the plane perpendicular to the propagation direction, and a significant simplification in the problem of beam alignment was achieved.

The experiment at 100 atm was then repeated with much more satisfactory results and the technique revealed previously unobserved structure (to be discussed in Chapter 5).

Data Acquisition and Reduction

Once the desired pump energy had been chosen and the pump and Stokes beams were properly aligned, the gain enhancement data was collected. This was done by using a Laser Precision energy meter (model RjP 735) to measure the output Stokes energy from the Raman amplifier as a function of the optical delay. The data was stored on disk

via a Hewlett-Packard Series 80 microcomputer. To ensure against anomolous data, three runs were taken at a given pump energy and averaged together point-by-point. The resulting average data file was then smoothed using the program GLATT as given in Appendix B. This program operated by Fast Fourier transforming[12] the data and throwing out high frequency components according to the smoothing parameter PTS, and transforming back. PTS was given a value of 1.0 in for all the data. This value eliminated the shot to shot noise while retaining the essential features of the curve as can be seen in Figure 4.

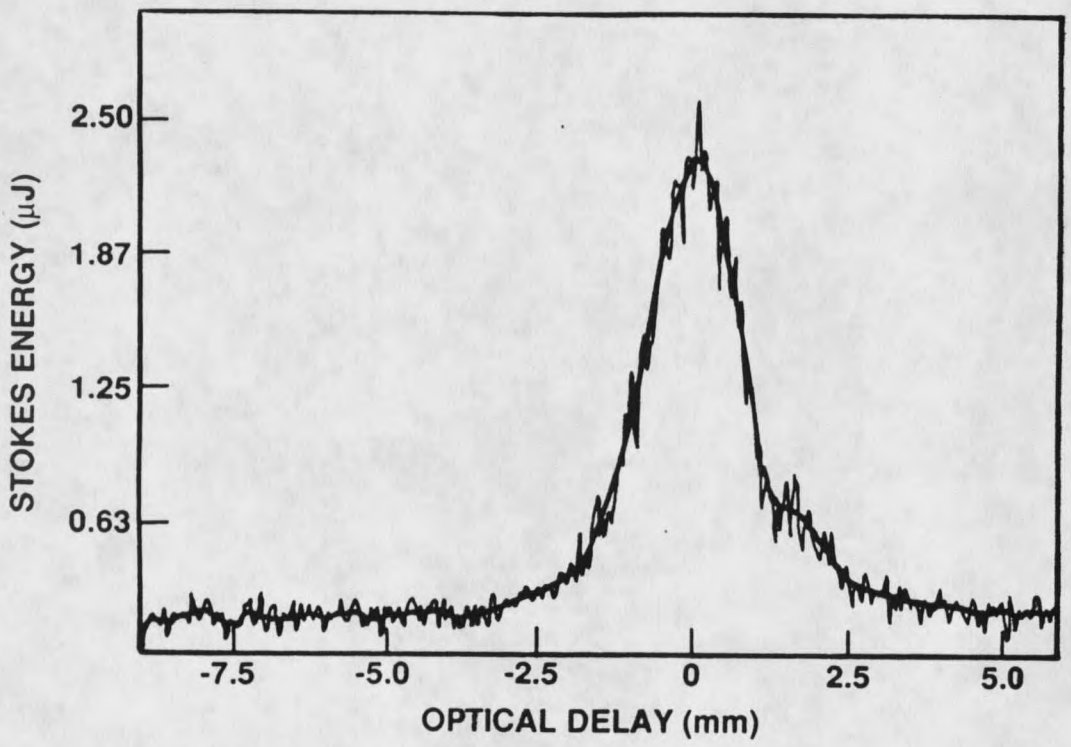


Figure 4. Typical optical delay data showing the effect of smoothing by the program GLATT. The jagged data is the average of three runs.

The first 100 points of the smoothed data were then averaged together to provide the uncorrelated energy while the maximum peak energy of the data provided the corre-

lated value. These values were converted to microjoules and their logarithims (base 10) were plotted versus the (corrected) input pump energy. The plots for the 100 and 10 atm data are shown in Figures 12 through 15 (see Chapter 5).

Upon the completion of data acquisition and reduction an error analysis was undertaken. Investigation revealed that the major sources of uncertainty in the experiment were due to beam misalignment and uncertainty in the linewidth measurement during a run. The uncertainty in Stokes energy caused by these two effects was 12.7% and 5%/cm^{-1} respectively. Additionally, smaller sources of error were noted in the uncertainty of the Stokes seed from run to run (14%) and a systematic error in the energy detectors (from specfications) of 5%. When added appropriately in quadrature the total uncertainty in the Stokes energy was found to be on the order of 15% for both the 10 and 100 atmosphere cases. This number was damped considerably upon plotting the Stokes energy logarithmically, the uncertainty becoming approximately $\pm$ 5%. The error bars are shown plotted, along with the data, in Figures 12-15.

CHAPTER FOUR

LINEWIDTH MEASUREMENTS

Introduction

To ensure optimal results in the gain enhancement experiment, it was necessary to monitor and control the laser linewidth in real time during data collection. In work prior to this[5], a spectrograph was used to monitor the linewidth but, its usefulness was limited because it lacked the resolution necessary to make accurate measurements at 308 nm. Additionally, accurate determination of the average linewidth for the well tuned laser was made by using a Mach-Zehnder interferometer. Although elegant, this method did not allow real time observation of the linewidth and consequently was not useful in controlling the laser during data collection. A solution to the problem of linewidth control was provided by the Fabry-Perot interferometer. In this chapter, the fundamentals of Fabry-Perot interferometry are discussed along with methods developed to determine the laser linewidth and the separation of the Fabry-Perot plates.

The Fabry-Perot Interferometer

The Fabry-perot interferometer is a spectroscopic instrument which, by virtue of its configuration, serves naturally as a wavelength filter. It consists of two highly reflective, optically flat plates separated by a distance d, and operates on the principle of multipass interference of the incident light with itself inside the cavity (i.e. between the plates). For

a beam of wavelength λ, incident on the plates at angle θ the idealized transmitted intensity is described by[6]

$$I_t/I_i = [1 + F\sin^2(\delta/2)]^{-1} \tag{4.1}$$

Here, I_i and I_t refer to the initial and transmitted intensities, F is the coefficient of finesse and is equal to $4R/(1-R)^2$, R being the plate reflectance. δ is the phase (angle) defined by $\delta = (4\pi n d \cos\theta)/\lambda$ where n is the refractive index of the cavity medium. When plotted, equation (4.1) is known as an Airy pattern and is mathematically denoted as $A(\delta)$ or $A(\theta)$. As shown in Figure 5, transmission maxima occur at $\delta = 2\pi m$ where m is an integer.

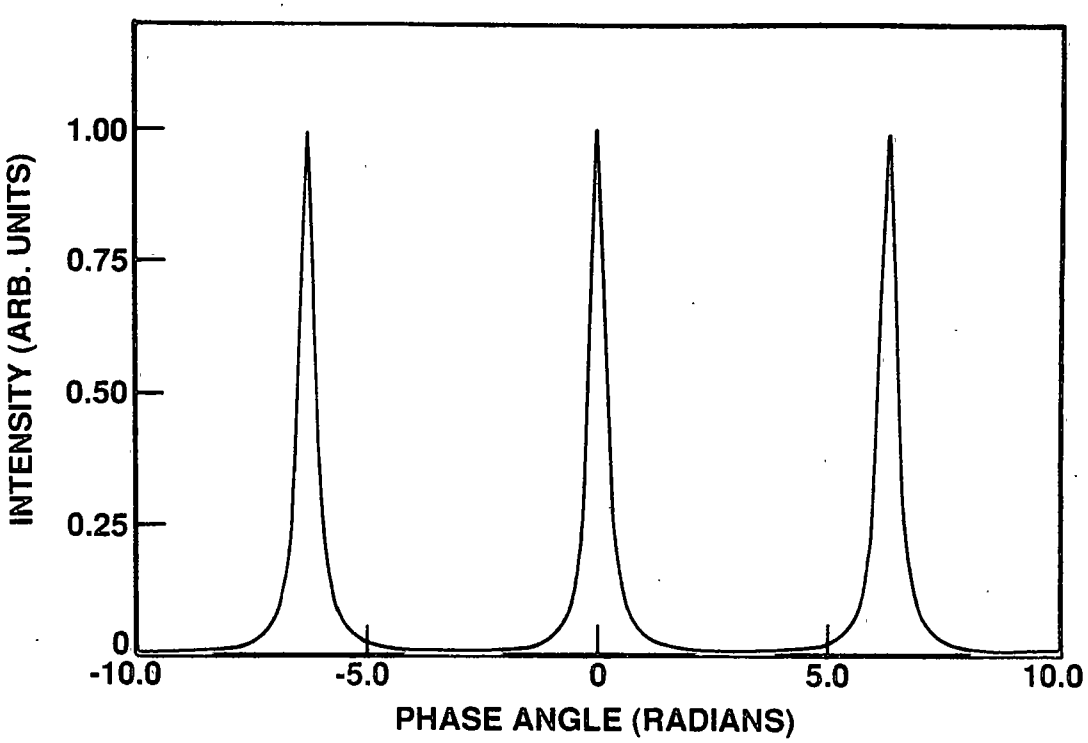


Figure 5. Theoretical output of an idealized Fabry-Perot as a function of phase angle δ, ($\delta = 4nd\cos\theta/\lambda$).

The full width at half maximum of the peak pattern is given by $\gamma = 4/\sqrt{F}$ and the finesse, defined as the ratio of peak separation to halfwidth is given by $f = \pi\sqrt{F}/2$. For non-monochromatic light, it is possible to have overlap of the m^{Th} order peak at wavelength λ_0 and the $(m+1)^{Th}$ order peak of a different wavelength. The difference in wavelength, $\Delta\lambda = |\lambda_0 - \lambda|$, when this condition occurs, is called the free spectral range of the instrument. In wavenumber units (cm^{-1}), it is given by $\sigma = 1/2nd$ with n denoting the refractive index. A quantity directly related to the free spectral range is the minimum resolvable bandwidth defined by the relation $\Delta\sigma = \sigma/f$.

If, as in this experiment, the incident light is a planewave and $\theta = 0$, then the interference fringes may be produced by placing a slight wedge angle α between the plates. At positions along the wedge where the plate separation is a half integral number of wavelengths ($d = m\lambda/2$), a linear fringe will appear with separation between the adjacent peaks corresponding to one free spectral range. This operation configuration is known as the Fizeau mode[6].

The Fabry-Perot used in this experiment was a Burleigh model RC150. Mounted in this frame were quartz (fused silica) plates having 97% reflectance and flatness (i.e. surface roughness) of $\lambda/200$. With this reflectance, the maximum attainable theoretical finesse is 103. Since it was desired to resolve spectral features of tenths of wavenumbers, a free spectral range of 8 wavenumbers was chosen. This gave a theoretical minimum resolvable bandwidth of 0.08 cm^{-1} and corresponded to a plate separation of 625 micrometers.

In actuality, several factors combine to reduce the maximum instrument finesse, and therefore decrease the resolution. The most important of these degradations are due to surface roughness and deviations from parallelism of the plates. The resulting total instrument finesse resulting from the above effects is given by[7]

$$f_T^{-2} = \Sigma f_T^{-2} \tag{4.2}$$

Specific values for the roughness and parallelism finesse may be calculated from the relations[7]

$$f_S = \lambda/2\sqrt{2}\,\Delta s \tag{4.3a}$$

and

$$f_P = \lambda/2\Delta s \tag{4.3b}$$

respectively. In the surface roughness formula Δs denotes the $\lambda/200$ plate flatness. This number, however, is typically stipulated at 546 nm and as a result, the finesse must be adjusted for the 308 nm wavelength. By assuming a linear relationship between the finesse and wavelength, a value of 40 was obtained for the roughness finesse at 308 nm. In the equation for parallelism finesse, Δs denotes the deviation from parallelism over the portion of the plate used. In practice, this number was obtained from the wedge angle (10^{-5} rad) and known width of the Fizeau fringe (750 μm). The resulting parallelism finesse was calculated to have a value of 21. Application of equation (4.2) then gave a value of 18 for the total instrument finesse and a corresponding minimum resolvable bandwidth of 0.42 cm^{-1}. As a check, the instrument finesse was measured in the laboratory by setting the plates 133 μm apart. This was done in order to eliminate resolving any spectral structure of the laser. The output of the interferometer was then digitized and stored as described below, and from this data the instrument finesse calculated. The results ranged from 15 to 30, and this fluctuation was probably due to the inability of the Fabry-Perot to keep from resolving some of the laser's broadband structure even at the smaller plate spacing. Hence, the experiment was inconclusive in obtaining a working value of the finesse. On the other hand, it was necessary to have an operational standard for use in calculating the laser linewidth. For this, a finesse of 30 was chosen based on

the assumption that the Fabry-Perot could operate at such parameters under optimal conditions.

Great emphasis need not be placed on the actual value of the finesse because neither it nor the laser linewidth is of critical importance in this work. In actuality, the Fabry-Perot functioned as a visual aid in keeping the laser well tuned during the course of the experiment, and therefore did not need extreme resolution. Operational finesse values between 15 and 30 proved adequate to monitor changes in the laser linewidth on the order of 10%.

To use the Fabry-Perot in this experiment, a portion of the pump beam was split off and brought to focus by a 1 m lens at the center of a spatial filter where it was "cleaned up", after which it was expanded and collimated by the -50 and 500 mm lens combination as shown in Figure 3. Upon passing through the interferometer, the resulting spectrum was incident on a linear photodiode array (EG & G Reticon series "G") and the signal observed on a Tektronix 2230 digital storage oscilloscope. The data was then transferred to an AT&T 6300 microcomputer for storage and analysis.

The Fabry-Perot plates were set near the desired plate separation of 625 μm using an optical measurement technique (to be discussed). The plates were then adjusted for operation in the Fizeau mode by placing a wedge angle of approximately 10^{-5} radians between them. This gave an interference pattern of two vertical lines across the diode array corresponding to one free spectral range. A typical set of data produced by this technique is shown in Figure 6.

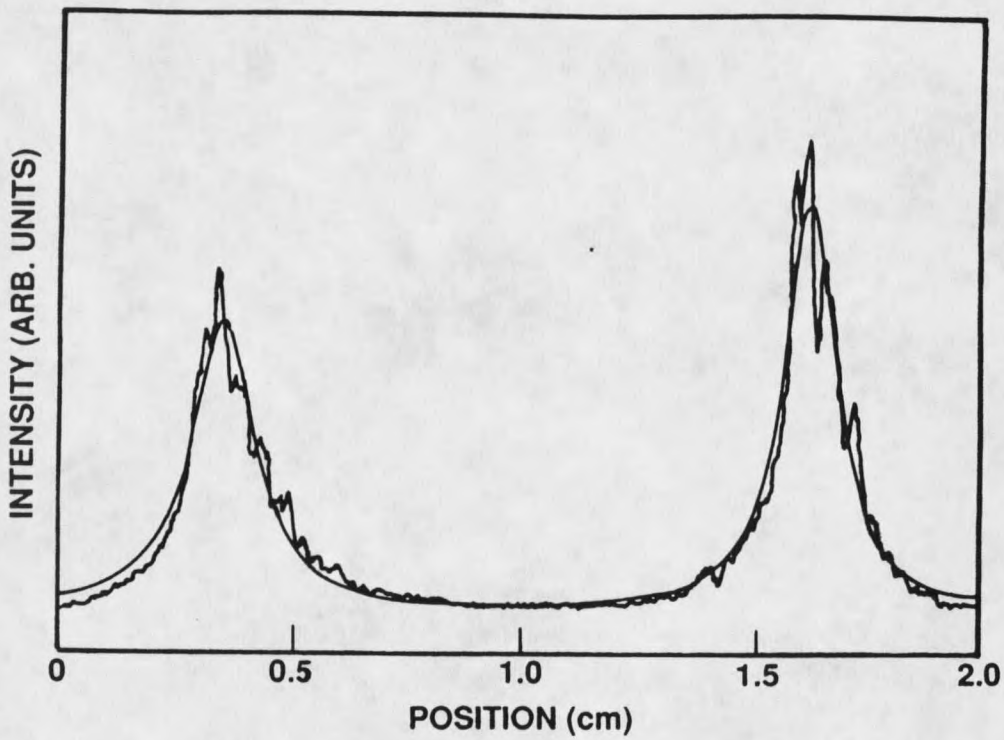


Figure 6. Typical digitized output of the Fabry-Perot operating in Fizeau mode. Also shown are the Lorentzian least squares fits to the peaks used in calculating the average laser linewidth.

The laser linewidth was calculated by least squares fitting the peaks of the digitized spectrum to a Lorentzian lineshape. The free spectral range and peak width (FWHM) in diode numbers were then calculated and converted to wavenumber units. The known value of the free spectral range in cm^{-1} was used to obtain the conversion factor.

To obtain a value for the average linewidth of the well tuned laser, sixty spectra were taken, their linewidths calculated and averaged together. From this data, the standard deviation was determined. The result was an average laser linewidth of 1.0 ± 0.1 cm^{-1}. This value compares well with that of 0.96 cm^{-1} reported by Rifkin[5] in previous work for the same laser.

Fitting the spectral peaks to Lorentzian lineshapes can be justified by expanding the Airy equation (4.1) using a small angle approximation. One obtains:

$$A(\delta) = (1 + \delta^2/\Gamma^2)^{-1} \tag{4.4}$$

Where $\Gamma = 2/\sqrt{F}$ is the half width at half maximum. This equation is clearly Lorentzian in form. The results of fitting the data to the generalized Lorentzian equation:

$$Y = H/(1 + (X - X_0)^2/\Gamma^2) + Y_0 \tag{4.5}$$

are also shown in Figure 7. Here H denotes the height, X_0 the X offset, Γ the width, and Y_0 the DC offset of the curve.

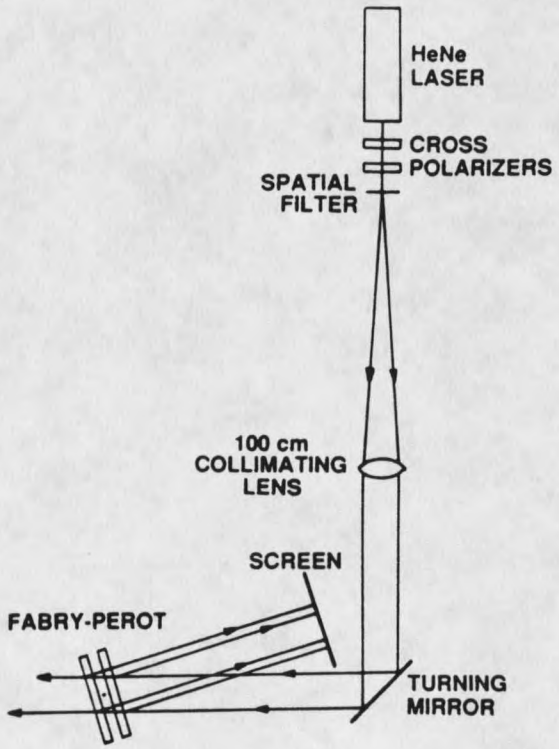


Figure 7. Schematic of apparatus used in measurement of the plate spacing. The Fabry-Perot is mounted on a rotatable stage and the back-reflected interference pattern is projected on the screen.

Because of the Fabry-Perot's ability to resolve the laser spectrum in real time it proved to be ideal for monitoring and control of the laser linewidth. It was possible to observe small changes in the linewidth and to easily adjust the laser for (near) optimal operation during the course of a run. This was important because, as will be discussed, changes in the value of the linewidth had a large impact on the gain enhancement observed.

Plate Separation Method

As the operating parameters of the Fabry-Perot were chosen for this work, it became clear that a highly accurate method for determination of the plate spacing was needed. This was due mainly to the small plate separation of 625 μm and the resulting high relative error which would arise from even small absolute errors in setting the plate spacing. This error would then propagate and ultimately affect the minimum resolvable bandwidth of the instrument, and if large enough, would have substantial effect on the measured laser linewidth.

An optical method for determination of the plate separation was developed based on the following considerations. The condition on the optical path length for constructive or destructive interference in a Fabry-Perot is[6]

$$n\lambda = 2d\cos\theta \tag{4.6}$$

where n is the order number, θ is the incident angle of the incoming light, and d is the plate separation. Now, if θ is allowed to change, equation (4.4) can be rewritten as

$$(n_0 - m)\lambda = 2d(1 - \theta^2/2) \tag{4.7}$$

where the small angle approximation on $\cos\theta$ has been used. Here n_0 denotes an order number common to all the angles. As a result, the equation relating θ to the new order number m is

$$\theta = (m\lambda/d)^{1/2} \tag{4.8}$$

By changing the angle of incidence and noting the change in order number, it is possible to obtain a value for d. This was achieved in practice by mounting the Fabry-Perot on a rotatable base such that the axis of rotation was coincident with the center of the air gap between the plates, and using a collimated Helium-Neon laser beam (Figure 7).

Because of the low reflectivity of the UV plates at the HeNe wavelength, it was necessary to use the Fresnel reflections from the plate surfaces to obtain an acceptable interference pattern. Thus, the method became known as the "HeNe backreflection technique". Initially, the plates were set to the desired separation and made "flat" (i.e. no wedge angle) using the Fabry-Perot's piezoelectric drives. The incident angle was zeroed by positioning the interferometer so that the HeNe beam reflected back on itself, and the order number was set to zero by adjusting the plate separation for destructive interference (i.e. a dark spot) as this was much easier to see than the constuctive interference peak. After zeroing the system, data was taken by rotating the Fabry-Perot through an angle corresponding to one order number. This procedure was repeated until the Fabry-Perot had been rotated through angles corresponding to 6 consecutive order numbers. The data was then fitted to equation (4.8) via a least squares fitting program and the value of the plate spacing returned. The method proved to be sensitive to changes in plate spacing on the order of 10 microns, and was quite accurate as well. The only error possible was in the measurement of the incident angle and it was determined that under careful operation this error was no greater than one minute of arc. Propagation of this error caused an

uncertainty of approximately 8 μm for plates separated by 625 μm or relative error of 1.3 percent. The results of a typical data set are shown in Figure 8. For this data set the plate separation was determined to be 628 microns.

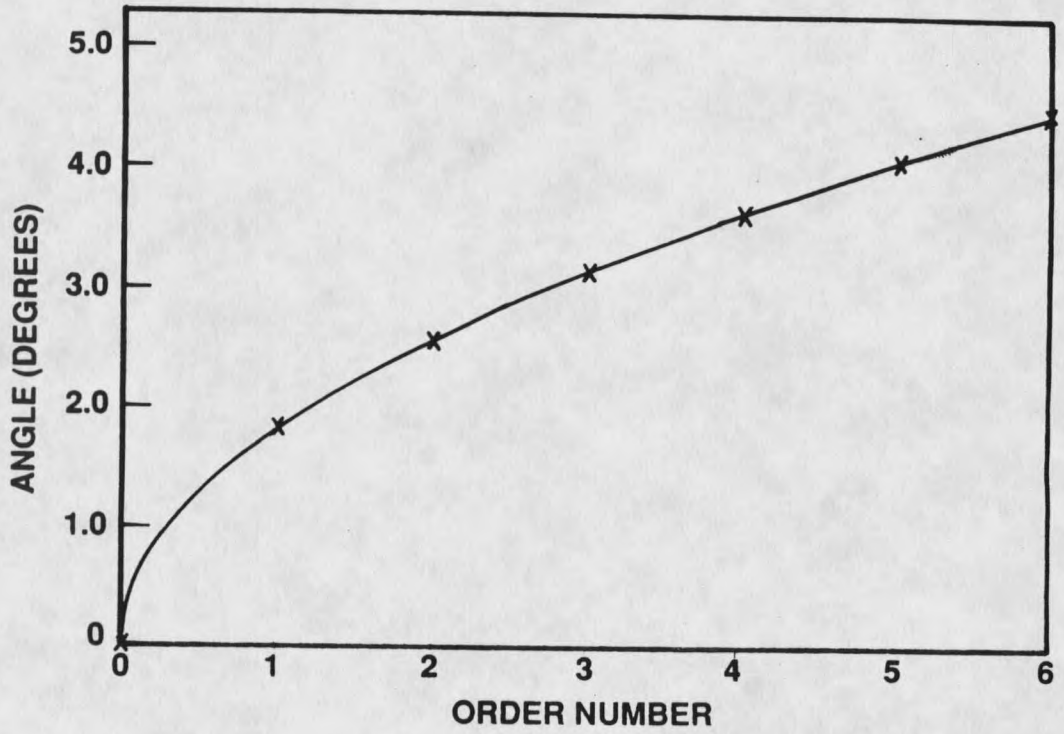


Figure 8. Fabry-Perot rotation angle as a function of order number and resulting least squares fit used in obtaining a value for the plate spacing, d. The plate spacing for this data was 628 μm.

CHAPTER FIVE

NUMERICAL ANALYSIS

Introduction

In this chapter, the numerical techniques used to model the experiment are presented. It should be emphasized from the outset that substantial effort was spent to build into the numerical models as much reality as possible. In doing so, much potentially dubious scaling of theory to fit the experimental data was avoided, and a much clearer picture of the physics involved allowed to emerge. To this end, pains were taken to produce source codes which gave results comparable, in an absolute sense, to the experimental data.

The first of these codes was LFELD which was used to calculate the laser and initial Stokes fields according to the fixed random phase model. The second program, RAMAN, numerically evaluated the integral solution for $E_S(z,\tau)$ (found in Chapter 2) as a function of the input pump energy.

In addition to LFELD and RAMAN, three other programs were used in this work. They were RAMCOR, AVEFIL2, and DEVIATE. These programs played supplemental/supporting roles and will be discussed at appropriate places in this chapter. The background theory and mathematical manipulations for each of these programs will be presented in their respective sections. All these programs were composed in MICROSOFT FORTRAN, and tested on NEC APCIII microcomputers. For the sake of speed, the working code was uploaded to the campus VAX cluster where the bulk of the

computing took place. The computer language of choice for this work was FORTRAN as it is the most widely used scientific programming language, and also because of the ease with which it can deal with the complex arithmetic which is prevalent throughout the computations. Beyond these considerations, the particular language used is not particularly important and so the source codes are relegated to Appendix B.

Modeling the Broad-band Laser

The first step in modeling the experiment is to generate the broad-band laser pulse. This was done using the fixed random phase model. The essential features of this model are now presented.

The fixed random phase model is an attempt to represent a gas lasing medium excited by electrical discharge as is the case with the XeCl excimer laser used in the experiments. The medium consists of a large ensemble of atoms which emit according to $E_n = A_n \exp(-i\omega t)$ into a large number of (frequency) modes as dictated by a large number of line broadening mechanisms. Such mechanisms include collisional dephasing, Doppler broadening, and the linewidth characteristics of a medium with many closely spaced excited vibrational levels as is the case with XeCl. These broadening mechanisms combine to give the frequency spectrum an overall lineshape which was taken to be Lorentzian in this work.

The chaotic nature of the excitation process (electrical discharge) also dictates that the individual atoms emit photons at different times, or equivalently with different, random phases. The electric field finally emitted by the laser is the sum of the individual fields produced by the atoms, weighted by the Lorentzian frequency distribution. Mathematically this can be written as

$$E_{total} = \sum_{n=-N}^{N} A_n e^{-i[(\omega_0 + \delta n)t + \phi_n]} \tag{5.1}$$

Here, ω_0 denotes the central frequency of the mode distribution, δ the mode spacing, n the number of modes away from ω_0, and ϕ_n a random phase between 0 and 2π. The amplitude A_n is weighted according to the Lorentzian intensity distribution, that is

$$A_n = \frac{1}{[\Gamma_L^2 + (n\delta)^2]^{1/2}} \frac{1}{\sqrt{\sum A_n^2}} \tag{5.2}$$

Here, the $(\sum A_n^2)^{-1/2}$ term is for normalization purposes and any other factors which would normally appear in the Lorentzian have been absorbed into A_n on the left side of equation (5.2). Implementation of these ideas was achieved in the program LFELD. First, the essential start up parameters were input by the user. They consisted of the number of modes (determined to be 708 by chopping the Lorentzian at the $1/e^2$ point), the mode spacing (0.0035 cm^{-1}) which was determined from the lasers cavity length L through the relation 1/2L, the halfwidth of the Lorentzian laser envelope (1 cm^{-1}), and a Stokes field scaling factor for use in calculating the energy of the Stokes pulse, and finally a random number seed for use in generating the phases. The program first calculated the random phases, then the weighted amplitudes. Next, the pump and Stokes fields were calculated (in the subroutine FIELDS) according to the prescription

$$E_L = \sum_{n=-N}^{N} A_{Ln}[\cos(n\delta t + \phi_n) + i\sin(n\delta t + \phi_n)] \tag{5.3a}$$

$$E_S = \sum_{n=-N}^{n} A_{Sn}[\cos(n\delta t + \phi_{Sn}) + i\sin(n\delta t + \phi_{Sn})] \tag{5.3b}$$

The rest of LFELD consisted of calculating $p(t) = \int |E_L(t')|^2 dt'$ which was normalized to 1 for reasons to be discussed in the next section, and calculating the Stokes seed energy.

In principle, LFELD appears to be a straightforward program by which to generate the fields. There are, however, some subtleties which need to be considered. First, as is

typical in numeric calculations, the electric fields were generated only at discrete points in time. It is then fair to ask how many intervals per unit time are needed to "follow" the pulse. An approximate answer is obtained by considering the beat frequency of the envelope: $\cos(\Delta\omega)$ where $\Delta\omega$ refers to the 1 cm^{-1} linewidth of the laser. This corresponds to 188 ns^{-1}. Allowing the envelope one half an oscillation i.e. $(\cos(\Delta\omega) = \pi)$ gives a minimum interval density of 188 intervals/ns. In the computations, a value of 200 intervals/ns proved adequate to follow the pulse and was used throughout the work (Little accuracy was gained in using higher interval densities and caused excessive computing time). A typical intensity profile generated by this program is shown in Figure 9.

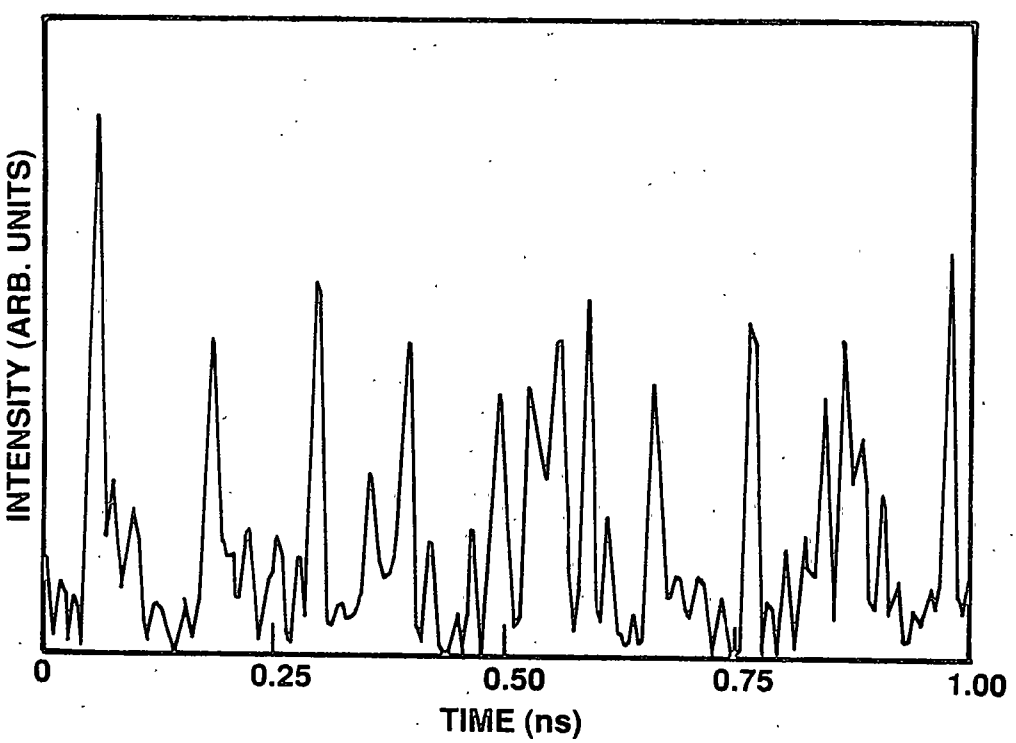


Figure 9. Typical electric field produced by the program LFELD using the fixed random phase model. A minimum of 188 points/ns is needed to "follow" the pulse.

The second issue which is not initally apparent is that this form of the fixed random phase model represents a temporal square pulse, i.e. the laser turns on at time t = 0, operates with constant power to time $t = \tau$, then shuts off. In fact this is not representative of the real laser pulse (see Figure 10). It is possible, however, to build into LFELD the capability to modify the total electric field to any desired temporal profile. Lack of time prohibited investigation into this "second order" modification of the theory. A number of authors,[2,3,32] however, have investigated the effect of arbitrary pulse shape, and the possible implications will be discussed later in Chapter 6. Having discussed the generation of the fields, it is now appropriate to discuss the numeric evaluation of the integral solution.

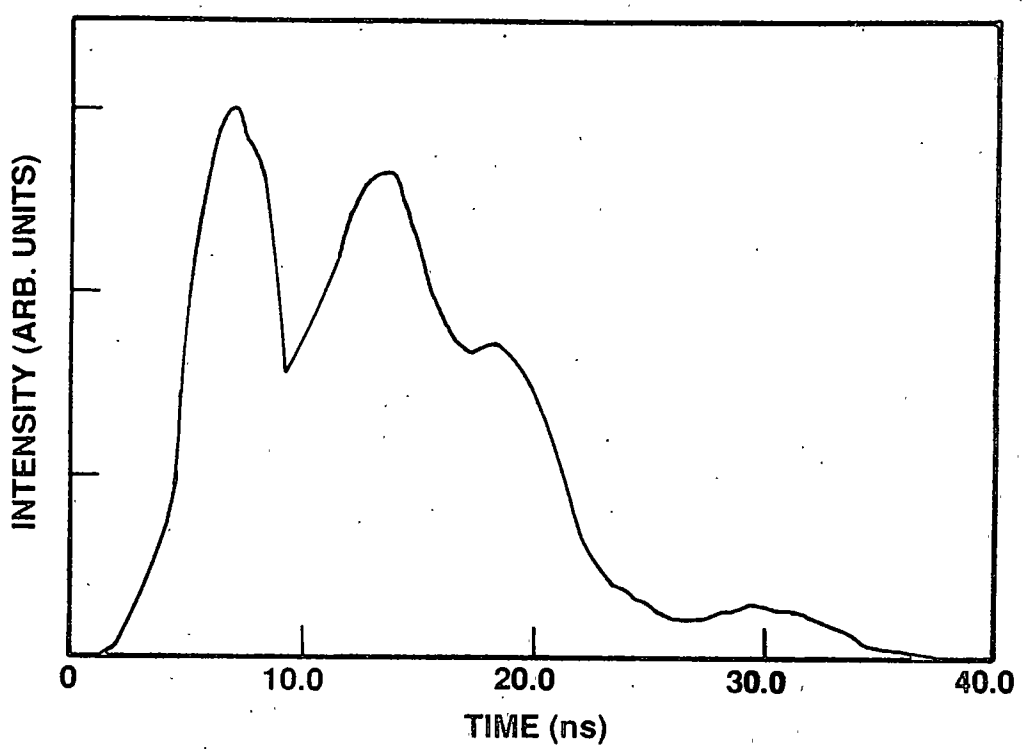


Figure 10. Typical temporal profile of the XeCl laser output. The square pulse corresponding to equal peak height was 13.5 ns in duration.

The Riemann Integral

In this section, the methods used for evaluation of the Stokes field solution are presented. Because the fields are stored in arrays corresponding to discrete time intervals, evaluation of the integral may be done by a straightforward trapezoidal algorithm. There are, again, a number of mathematical devices used at this stage which merit discussion.

From the outset, the experimental quantities of importance were the laser and Stokes energies, hence the program RAMAN was required to generate a so-called gain curve i.e. the Stokes energy as a function of input pump energy to match the experimental data. In addition, the connection between the input pump energy and the gain coefficient[3] $G = 2\kappa_1\kappa_2 E_L^2 z/\Gamma$ was necessary. The following discussion describes how these features were incorporated into the program.

From the previous chapter the equation for the Stokes field is

$$E_S(z,\tau) = E_S(0,\tau) + \sqrt{\kappa_1\kappa_2 z}\, E_L(\tau) \int_0^\tau \frac{E_L^*(\tau')E_S(0,\tau')}{\sqrt{p(\tau)-p(\tau')}} e^{-\Gamma(\tau-\tau')} I_1[\sqrt{4\kappa_1\kappa_2 z(p(\tau)-p(\tau'))}]\, d\tau' \quad (5.4)$$

where $p(\tau) = \int_0^\tau |E_L(\tau')|^2 d\tau'$. In order to mimic the actual experiment as closely as possible with the computer model, it was necessary for the program to calculate the amplified Stokes energy as this was the experimentally measured quantity. This in turn required that the amplified Stokes field be known at discrete times between 0 and τ. In RAMAN this was done using a loop in which the time was incremented, the Stokes integral evaluated up to that time, and repeated until time had been incremented to the desired pulse length. Once generated for times such that $0 < t \leq \tau$, the Stokes field was integrated to obtain the energy according to the relation

$$\Lambda_S = \varepsilon_0 c \pi \omega_0^2 \int_0^\tau |E_S|^2 d\tau' \quad (5.5)$$

The factor $\pi\omega_0^2$ is the spatial area of the pulse (which is assumed to be Gaussian) and ω_0 is the beam waist, c is the speed of light, and ε_0 is the permittivity of free space. Equation (5.5) arises from considerations of energy flux and intensity[6]. Further, it was necessary for the program to be able to generate the Stokes energy as a function of the input pump energy. This was achieved by writing equation (5.4) based on the following considerations. First $p(\tau)$ was rewritten as

$$p(\tau) = E_L^2 \int_0^{\tau} |\, E_L(t) \,|^2 \, dt = E_L^2 \mathrm{p}(\tau) \tag{5.6a}$$

with $p(\tau)$ constrained to be normalized, that is

$$\int_0^{\tau} |\, E_L(t') \,|^2 \, dt' = 1 \tag{5.6b}$$

Going further, an adjustable parameter C was introduced via the relation $C = \sqrt{\kappa_1 \kappa_2 z E_L^2}$ and equation (5.4) becomes

$$E_S(z,\tau) = E_S(0,\tau) + C E_L(\tau) \int_0^{\tau} \frac{E_L^*(\tau') E_S(0,\tau')}{\sqrt{\mathrm{p}(\tau) - \mathrm{p}(\tau')}} e^{-\Gamma(\tau - \tau')} I_1[\sqrt{4C(\mathrm{p}(\tau) - \mathrm{p}(\tau'))}]\, d\tau' \tag{5.7}$$

So, it can be seen that adjusting C is tantamount to adjusting E_L^2 and hence, the input pump energy. In order to calculate the laser energy from C, equations (5.5) and (5.6) were used to obtain

$$\Lambda_L = \frac{\varepsilon_0 c \pi \omega_0^2 C^2}{\kappa_1 \kappa_2 z} \int_0^{\tau} |\, E_L \,|^2 \, d\tau' \tag{5.8}$$

Note, however, that the integral was normalized. Using this fact the laser energy was written as

$$\Lambda_L = \frac{\varepsilon_0 c \pi \omega_0^2 C^2}{\kappa_1 \kappa_2 z} \tag{5.9}$$

From (5.9) it can be seen that it was necessary to have accurate values for the coupling constants $\kappa_1\kappa_2$. A numerical value was obtained based on the equation[8]

$$\kappa_1\kappa_2 = \frac{\Gamma c\,\alpha}{16\pi} \tag{5.10}$$

α is known as the plane wave gain coefficient and was found to have a value of 6.6 ± 0.8 x 10^{-9} cm/W [9]. It must be noted that equation (5.10) is given in Gaussian units, and to convert to MKS units it is necessary to multiply by $4\pi\varepsilon_0$ [10]. Equation (5.10) then becomes

$$(\kappa_1\kappa_2)_{MKS} = \frac{\varepsilon_0 c\,\Gamma\alpha}{4} \tag{5.11}$$

Using a value for Γ at 10 atm of 244 MHz (HWHM)[11], $(\kappa_1\kappa_2)_{MKS}$ has a value of 6.68 X 10^{-5} m/V^{2}s. Since the Raman linewidth scales linearly with increasing pressure from 1 to 100 atm[9], the value for Γ at 100 atm pressure can be taken to be 2440 MHz (HWHM) and results in a value for the product of the coupling constants at 100 atm of 66.8 X 10^{-5} m/V^{2}s.

The program RAMAN operated in the following manner. Initially the program loaded the appropriate files generated by LFELD. These files included a parameter file, files for the pump and Stokes fields, and a file for the pump energy as functions of time. Next, the gain range desired was input by the user, along with the number of points desired along the gain curve. From this, the values of C were calculated. The appropriate values of the fields and pump energy were transferred to the subroutine INTGRND where the integrand of equation (5.7) was calculated. Embedded in this subroutine was a function to calculate I_1, the 1st order Bessel function[18]. At this point it is clear why p(t) was normalized to 1. This is because the argument of the Bessel function is the difference between $p(\tau)$ and $p(\tau')$. This difference can be scaled to be less than 1 multiplied by an appropriate constant i.e. $p(\tau) - p(\tau') = const$ X [p(τ) – p(τ')]. It turns out, fortuitously,

that the scaling constant is just the parameter C. This scaling also has the effect of keeping the Bessel function from "blowing up" when τ gets large thus, increasing the precision of the computations.

From this point, the rest of RAMAN consists of calculating energies according to equations (5.5) and (5.8) and writing them to appropriate output files.

Program Testing

A goal of this project was to compare theory and experiment for four cases: 10 and 100 atm correlated gain (corresponding experimentally to zero optical delay) and 10 and 100 atm uncorrelated data corresponding to a large optical delay between pump and Stokes beams. Since the theory had been previously validated at 100 atm by Rifkin[5], the uncorrelated 100 atm case was chosen as the test bed case for the program. In this case, a number of theoretical predictions could be tested as computational "boundary conditions" for the program. Among them were (1) transiency effects when pulse length were on the order of the medium's coherence time, (2) behavior of the gain curves relative to power changes of the pulse, and finally, (3) evolution of correlated pump and Stokes from two initially uncorrelated fields with increasing gain.

The "zeroth order" test of RAMAN was to generate a gain curve qualitatively similar to those predicted by theory. To do this, uncorrelated pump and Stokes fields were generated having long pulse times compared to the coherence time of the medium (T = 0.6 ns at 10 atm.) and running RAMAN with gain ranging from 0 to 75 which corresponded to increasing the incident pump energy. This yielded a gain curve in qualitative agreement with theory. Additionally, this gain range was also used in subsequent computations at both 10 and 100 atm.

To test the effect of transiency, the pulse duration of the fields was adjusted to be comparable to the coherence time of the medium at 10 atm. In this case a number of runs were made using uncorrelated fields generated using different random number seed pairs with approximately 50% of the runs exhibiting transient behavior. A typical transient result is shown in Figure 11.

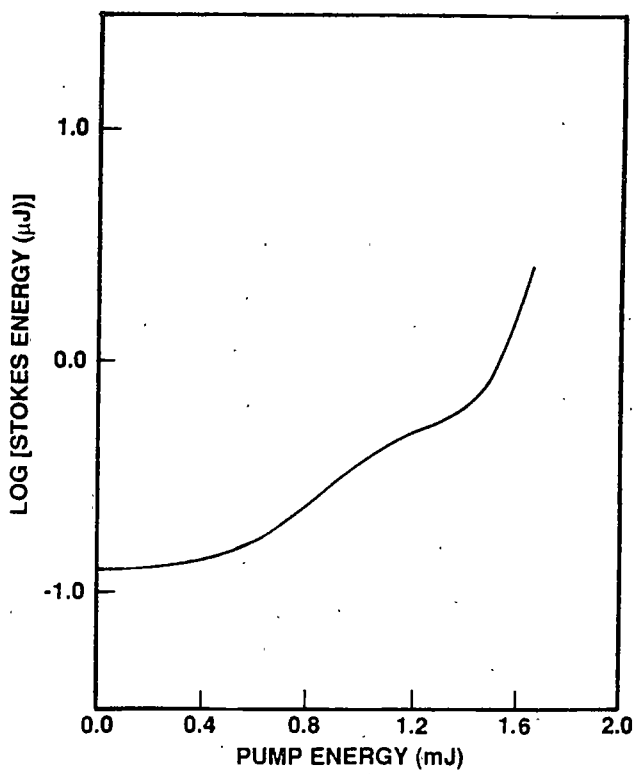


Figure 11. Numerical gain curve showing transient behavior. Transient behavior results from pulse times comparable to the coherence time ($1/\Gamma$) of the medium.

At this point in the testing, the need for reduced computing time became clear. To reduce the time necessary to generate a curve it was hypothesized that the initial pulse time could be reduced by some known factor, thus increasing the power of the pulse, the curve generated, and then scaled back to the initial power by adjusting the pump energy

scale of the gain curve. To test the hypothesis, gain curves for uncorrelated fields (having the same random seed pair) of 5 and 10 ns were generated, with the 5 ns curve being scaled by a factor of 2 in pump energy. When compared, the gain curves matched quite well. In an attempt to find the lower limit on the scaling process, the procedure was repeated for successively shorter pulse times. At 100 atm no significant changes were observed for pulse times as short as 0.5 ns relative to a target curve of 10 ns. There were, however, significant deviations from the 10 ns curve at 10 atm for times below 5 ns. Consequently, a lower limit of 5 ns was used for both the 10 and 100 atm cases with scaling used as needed to fit the data. The method proved to give a 50% savings in computing time.

To further test the program, the theoretical prediction that an uncorrelated Stokes field will become correlated with the pump field as the gain is increased. RAMAN was modified to output the field intensity for both the pump and Stokes. Next, two uncorrelated fields were input and a single gain value was chosen with which the intensities were generated. This was repeated for a number of increasing gain values. Indeed, it was observed that the two fields became correlated.

The tests above indicated that RAMAN (and also LFELD) were performing the desired operations and could now be used in fitting the data.

Once RAMAN was tested to ensure proper operation, it was used to fit the experimental data. As mentioned earlier, the uncorrelated data was fit first. To do this it was necessary to generate uncorrelated pump and Stokes fields by running LFELD twice using different random number seeds. Next, the uncorrelated fields were run in RAMAN with gain ranging from 0 to 75.

The Stokes energy scaling was adjusted to give a seed energy of 0.1 μJ as in the experiment, and the initial pulse time was 5 ns. Based on scaling arguments from the previous paragraphs, freedom existed to scale the pulse time as needed to fit the data (as

long as τ was greater than or equal to 5 ns). Indeed, the pulse time was essentially the only free fitting parameter in the entire numerical process.

To compare theory to experiment, it was also necessary to account numerically for the statistical nature of the experiment. Since the laser is pulsed, it never generates the same field twice and as a result, the gain curve developed from the optical delay data is really a gain curve for the average of a large number of fields. Conversely, one can associate a gain curve with each shot and claim that the data is the result of averaging many gain curves together. This process can easily be duplicated numerically as well, and this is exactly what was done to fit the data.

Data Fitting

The method by which theory was fit to the experimental data was essentially the same for the correlated and uncorrelated cases with only slight differences between the two. In actuality, there are 3 cases to consider. First, the totally uncorrelated case corresponding experimentally to a large optical delay between the pump and Stokes fields. This also corresponds numerically to pump and Stokes fields generated using different random number seeds. Second, the totally correlated case which corresponds experimentally to zero optical delay between perfectly correlated pump and Stokes fields. Third, the case corresponding to partially correlated pump and Stokes fields. As mentioned in Chapter 3, the Stokes field arising from spontaneous emission becomes partially correlated with the pump field in the Raman generator. Although the gain in the generator is large, the fields can never become perfectly correlated because of the finite response/coherence time of the medium. The effect is more pronounced at 10 atm than 100 atm because the 100 atm response time (given by the reciprocal of the linewidth Γ) is

10 times smaller than at 10 atm. The shorter response time allows the medium to better follow the spiky envelope of the broadband pulse because any phase relationship built up between the medium and pulse is more quickly destroyed by collisional dephasing at the higher pressure, effectively shortening the "memory" of the medium, and thus allowing it to respond to the pulse faster. Since the medium is able to respond to the pulse better at high pressures it follows that the Stokes field generated will be more highly correlated.

To fit the uncorrelated data, 16 curves for each pressure were generated from fields 5 ns long using different random number seed pairs. Subsequently, the programs AVE-FIL2 and DEVIATE were applied to the gain curves to calculate the average gain curve and standard deviation. Next, the pump energy was scaled as needed to match the average gain curve to the data. In the 100 atm case, the pump energy scale factor was 1.3 corresponding to a pulse duration of 6.5 ns. For the 10 atm uncorrelated data, the scale factor was 1.85 giving a pulse time of 9.25 ns. The results for the uncorrelated case are shown in Figures 12 and 13.

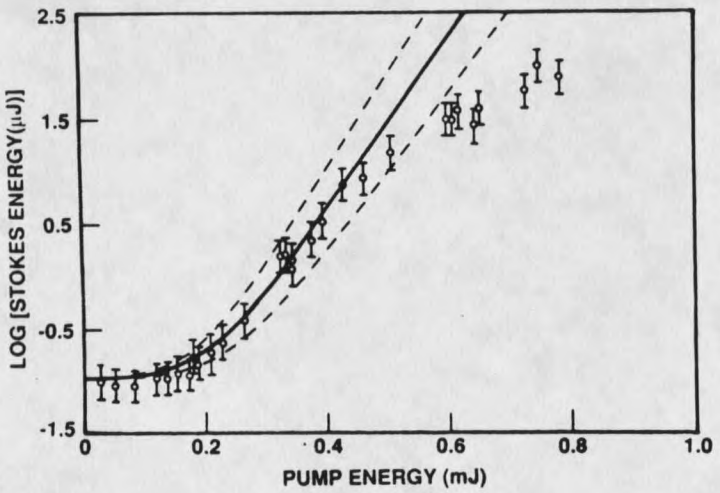


Figure 12. Numerical gain curves fit to 100 atm uncorrelated data. Shown is the uncorrelated ensemble average with statistical uncertainties. The numerical pulse duration was 6.5 ns.

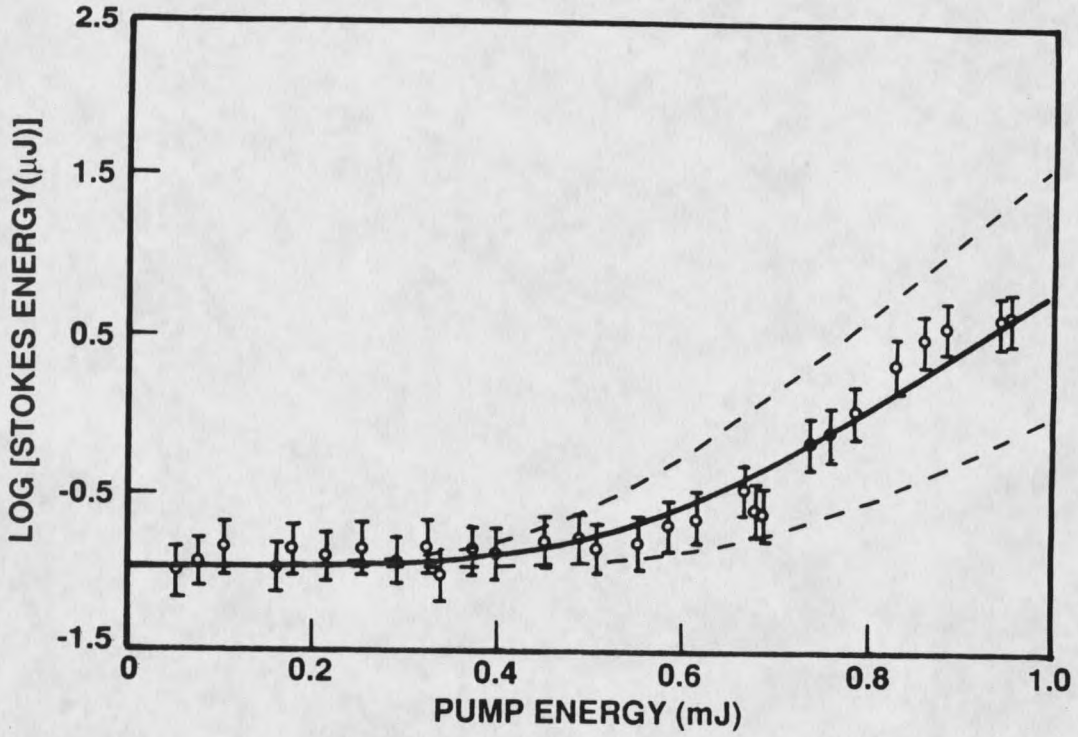


Figure 13. Numerical gain curve fit to 10 atm uncorrelated data. The curved line indicates the ensemble average with statistical uncertainties interpreted as vertical error bars. The pulse time used in computations was 9.0 ns.

To fit the totally correlated case, perfectly correlated 5 ns pump and Stokes fields were generated and scaled appropriately to match the slope of the experimental data in the region before depletion. Averaging was not needed in this case because each random seed used generated the same line. To match slopes at 100 atm, the pump energy was scaled by a factor of 1.1 giving a pulse time of 5.5 ns while at 10 atm, the scale factor was 1.8 corresponding to a pulse of 9.0 ns.

To fit partially correlated data, the procedure used for the uncorrelated data was applied with slight modifications. After the uncorrelated fields were generated, the program RAMCOR was applied to the Stokes field to generate the partially correlated field.

Essentially, RAMCOR was a modification of RAMAN having provisions for single gain values to be input and the Stokes field to be output. Once this was done, both the pump and Stokes fields were run in RAMAN and the resulting gain curves averaged as before.

To generate the proper correlation, gain values of 10 and 20 were used at 100 and 10 atm respectively. Also, the scale factors were the same as in the perfectly correlated case, giving pulse times of 5.5 ns at 100 atm and 9.0 ns at 10 atm. The results of these numeric calculations are shown in Figures 14 and 15.

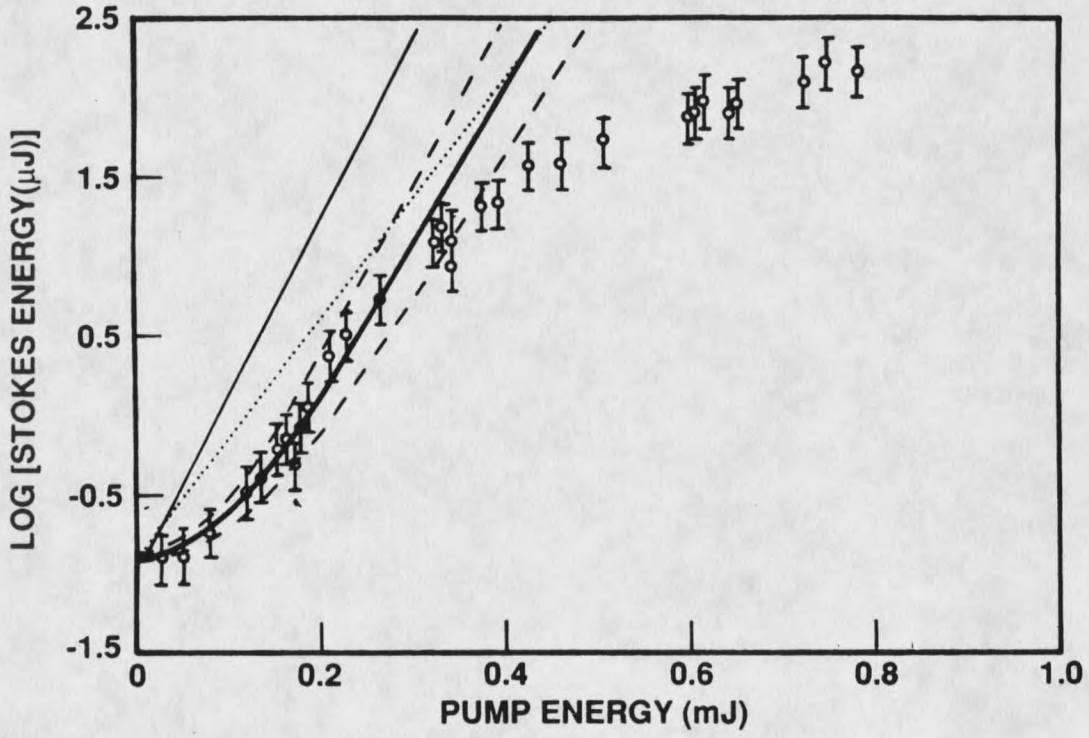


Figure 14. Numerical gain curves fit to 100 atm correlated data. Shown are the totally correlated (straight line) and partially correlated ensemble average curves. Additionally, the dotted line shows the theoretical result for totally correlated single mode gain. The dashed lines denote statistical uncertainties in the ensemble average. Both theoretical curves correspond to 5.5 ns square pulses.

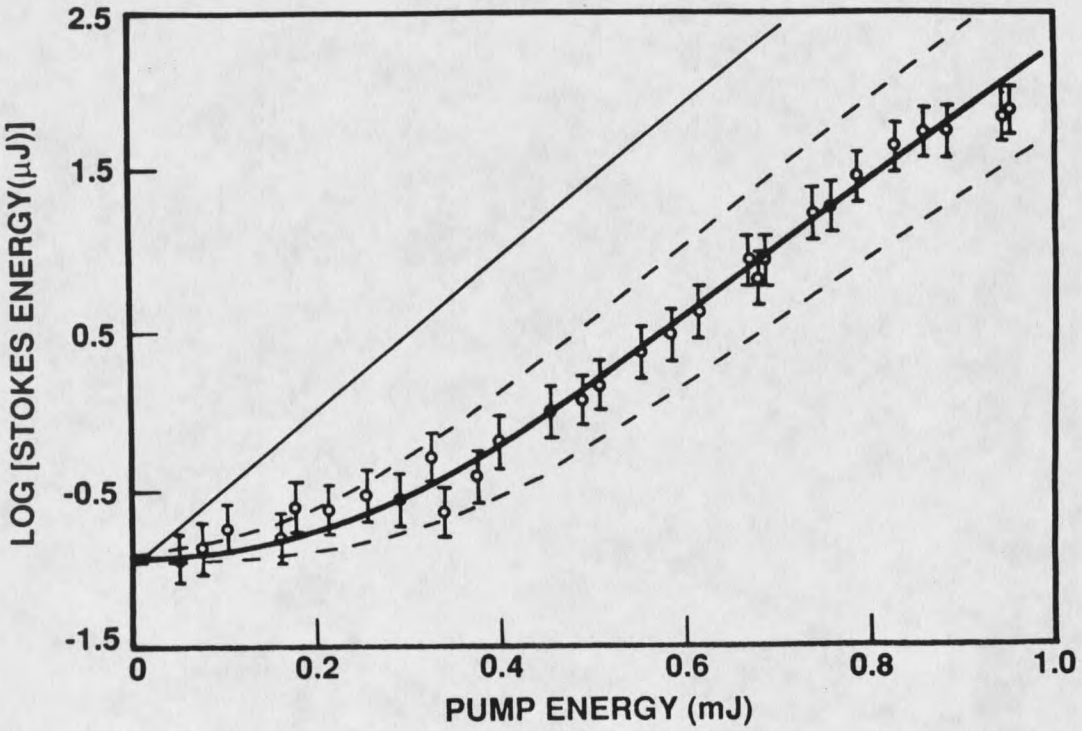


Figure 15. Numerical gain curve fit to 10 atm correlated data. Shown as a straight line is the monochromatic (totally correlated) case. The curved line indicates the ensemble average gain curve with statistical uncertainties. The numerical pulse length used was 9.0 ns.

CHAPTER SIX

ANALYSIS, INTERPRETATION, AND CONCLUSION

Introduction

In this chapter the theoretical/numerical results presented in Chapter 5 are analyzed and interpreted. As can be seen from Table 1 below, none of the pulse times derived from the data fits are the same. The physical significance of this demands interpretation and leads immediately to three areas of consideration. First, similarities between this work and that of Rifkin[5,26] will be examined with comments made pertaining mainly to the data fitting techniques used in each project. Second, a comparison of results between the 10 and 100 atmosphere cases will be undertaken. This discussion will center around differences in correlation between the incident pump pulse and the Stokes field produced by the coherence of the medium. The coherence of the medium will change due to the different Raman linewidth of the medium when the pressure is lowered. This discussion will be followed by one considering the differences in pulse times between the correlated and uncorrelated data at single pressures. Beforehand, however, a short description of the experimental data will be given. Subsequently, concluding remarks regarding the temporal square pulse model and its impact on the results of this thesis will be made.

Pressure (atm)	Field Correlation	Pulse Length (ns)	Percent Difference
100	Correlated	5.5	--
	Uncorrelated	6.5	18
10	Correlated	9.0	--
	Uncorrelated	9.3	3

Table 1. Pulse times derived from numerical fits to experimental data using the temporal square pulse model.

Experimental Data Characterization

The experimental data shown in Figures 12 through 14 exhibit consistent similarities. Typically, the uncorrelated data showed non-exponential gain characteristics at low input pump energies, but became exponential as pump energy was increased until the onset of pump depletion. Specifically, the 10 atmosphere data exhibited the largest range of non-exponential behavior becoming so only at 0.5 mJ and rolling off at 0.9 mJ pump energy. The 100 atmosphere data by comparison was exponential in the range 0.2 to 0.5 mJ.

By contrast, the data for correlated pump and Stokes fields was much more exponential in behavior. The 10 atmosphere correlated data was exponential in the range between 0.3 and 0.8 mJ where the roll off due to pump depletion occurred, while at 100 atm the exponential behavior occurred between 0.1 and 0.4 mJ input pump energy.

Comparison to Previous Work

As stated in the introduction to this thesis, the basic goal of this research was to resolve issues from previous work by Rifkin[5,26] who used essentially the same experimental apparatus. Specifically of interest was the verification of theory for the experimental data at 10 atmospheres pressure. For all intents and purposes the apparatus and data collection procedures were identical save for the modifications described in Chapter 3. The improved beam alignment technique in conjunction with the lower input Stokes seed energy (0.1 vs. 0.4 microjoules) revealed the non-exponential behavior at low pump energies for the 100 atmosphere correlated data which was not seen in Rifkin's data. This feature was attributed to partial correlation between pump and Stokes fields at low pump energies. Data from both experiments proved to be comparable as well, with Rifkin's data exhibiting approximately the same gain as seen in this project over the input pump energy range of 0 to 1.0 mJ.

The major differences between the two projects occurred in the realm of data fitting. In his work Rifkin derived a 15.3 ns square pulse of equal peak height and energy as the actual laser pulse for a temporal benchmark, whereas in this work such a pulse was found to be 13.5 ns long. Rifkin also states that the theoretical peak power density calculated using the 15.3 ns benchmark was only 71% of the actual measured value. Calculation of an equivalent square pulse based on the *measured* peak power density yields a value of 10.9 ns. Assuming the same situation to hold for the 13.5 ns square pulse calculated in this work (see Figure 10) a similar calculation yields a pulse duration of 9.6 ns, or essentially the pulse time determined from the 10 atmosphere data fits. Unfortunately, measurement of the peak power density was not repeated in this work so verifica-

tion was not possible.

In both projects the base pulse length used in the computer codes was essentially the same (4.7 ns for Rifkin's work compared to 5 ns for this work). It is unclear, however, whether Rifkin used any scaling arguments in his data fitting to reconcile the 4.7 ns computational pulse length with the 15.3 ns square pulse benchmark. If the scaling methods used in this thesis are applied to Rifkin's 10 atmosphere theory it can be seen that a longer pulse duration not only provides a better fit to data, but will also bring his computational pulse time more in line with the effective pulse duration of 10.9 ns calculated above. Additionally, large amounts of computing power were unavailable to Rifkin at the time of his data fitting, and so consequently he was unable to provide any statistics associated with the gain curves generated from random pump and Stokes fields. Verification of the statistical nature of the gain curve provided by this work suggests a partial explanation for the data fits obtained by Rifkin. It was observed that through fortuitous choice of the seed value used to generate the pump and Stokes field it is possible to obtain a good data fit for a single curve at one pressure and not the other. It is possible that this was the case in previous work, although it is unlikely that this phenomenon alone could account for the lack of fit in Rifkin's 10 atmosphere theory.

Comparison of 10 and 100 Atmosphere Results

The data presented in Table 1 indicate that the pulse times derived from fitting the 10 atmosphere data were almost twice as long as for the 100 atmosphere data fits. From a qualitative standpoint this can be attributed to the increased transiency of the medium at the lower pressure. In essence the coherence Q of the medium will not be as sharply

peaked in time as the input pump pulse. In fact if the medium is very transient it may contain only large scale features similar to the input pulse. As a result the Stokes field produced by this coherence will also not have the sharpness of the broadband pump pulse. Since the gain is basically exponential it immediately becomes clear that such a rounded off Stokes pulse will experience lower gain compared to a sharply spiked, well correlated one. Conversely, it will require more pump energy for the rounded Stokes pulse to acquire the same gain as a sharply spiked one. This effect was observed in the experimental data, and was manifested in the data fits as corresponding to a longer pulse time.

Comparison of Correlated and Uncorrelated Data

The third area of interpretation to be discussed is in the differences between derived pulse times for the correlated and uncorrelated fits at single pressures. For the 10 atmosphere case the pulse times differ by only 3 percent, while at 100 atmospheres the correlated time differs from the uncorrelated by 18 percent. During the course of this work no physical reason was found which could adequately account for the agreement at 10 atmospheres and the differences at 100. The large percentage difference in the 100 atmosphere case can be explained by taking into account the uncertainties in the theoretical curve and experimental data. It was found that if the uncorrelated data were scaled to yield a pulse time of 5.5 ns the statistical uncertainty was still large enough to encompass most of the experimental data and still yield a reasonable fit. Given the number of uncer-

tainties present in both the experiment and the numerical calculations the 18 percent difference between the correlated and uncorrelated cases is quite reasonable, while the 3 percent difference in the 10 atmosphere case can be considered somewhat fortuitous.

Comments on the Temporal Square Pulse Model

In this section a number of aspects of the temporal square pulse model are discussed. Basically the model has two adjustable parameters built in: the amplitude of the pulse, and its duration. Unfortunately it is these two parameters which give the model the flexibility to fit gain curves generated by arbitrarily complex temporal profiles. As a result little useful information is obtained by using the two parameter model. Reduction to a single fitting parameter may be achieved if the other is constrained to correspond to a physically meaningful quantity. For example the height of the square pulse could be set equal to the peak height of the actual laser profile, or normalized to unity as was done in this work, while the pulse length was taken as the adjustable parameter. As has been discussed in this and the preceeding chapter the one parameter model still has enough flexibility to fit the experimental data, and therefore arbitrarily complex temporal profiles. This situation is still unsatisfactory to a degree because the adjustable parameter model does not constitute a very rigorous test of theory. An argument for its use can be made on the basis of comparison to previous work using the same or similar model as in the case of Rifkin although ideally an absolute fit of theory to experimtent is desired. This demands that there be *no* adjustable parameters in the numerical analysis. This in turn requires that the actual temporal as well as spatial profiles of the system under consideration be incorporated into the analysis in a manner similar to that of Duncan et. al.[32].

This criterion renders the temporal square pulse model inadequate for a rigorous solution to stimulated Raman scattering in broadband lasers. Unfortunately this was not realized at the time of data fitting when the computer analysis could have been adapted to the zero parameter model. As a result a more definitive answer to the question of validity of the theory for stimulated Raman scattering in 10 atmosphere hydrogen is not possible in this work. The results of this work, however, clearly indicate that the effects of transience and pulse shape need to be included for a definitive comparison between broadband theory and experiment.

REFERENCES CITED

1. C. W. Wang, "Theory of Stimulated Raman Scattering," Physical Review, 182, 482 (1969)

2. R. L. Carmen, R. Shimizu, C. S. Wang, and N. Bloembergen, "Theory of Stokes Pulse Shapes in Transient Stimulated Raman Scattering," Physical Review A, 2, 60 (1970)

3. M. G. Raymer, J. Mostowski, J. L. Carlsten, "Theory Stimulated Raman Scatttering with Broadband Lasers," Physical Review A, 19, 2304 (1979)

4. M. G. Raymer, J. Mostowski, "Stimulated Raman Scattering: Unified Treatment of Spontaneous Initiation and Spatial Propagation," Physical Review A, 24, 1980 (1981)

5. J. Rifkin, "Gain Enhancement in a XeCl-Pumped Raman Amplifier," Masters Thesis, Montana State University, Bozeman, MT (1987)

6. E. Hecht, A. Zajac, *Optics*, Addison-Welsley Publishing Company, Reading, Massachusetts, 1974

7. E. Moore, C. Davis, M. Coplan, *Building Scientific Apparatus: A Guide to Design and Construction*, Addison-Wesley Publishing Company, Reading, Massachusetts, 1983

8. D. C. MacPherson, R.C. Swanson, J. L. Carlsten, "Stimulated Raman Scattering in the Visible with a Multi-Pass Cell," IEEE Journal of Quantum Electronics, in press, (July 1989)

9. W. K. Bischel, M. J. Dyer, "Wavelength Dependence of the Absolute Raman Gain Coefficient for the Q(1) transition in H_2," Journal of the Optical Society of America B, 3, 677 (1986)

10. J. D. Jackson, *Classical Electrodynamics*, John Wiley and Sons, 2nd Edition, New York, 1975

11. W. K. Bischel, M. J. Dyer, "Temperature Dependence of the Raman Linewidth and Lineshift for the Q(1) and Q(0) Transitions in Normal and Para-H_2," Physical Review A, 33, 3113 (1986)

12. W. H. Press, B. P. Flannery, S. A. Teukolsky, W. T. Vetterling, *Numerical Recipes*, Cambridge University Press, Cambridge, Massachusetts, 1986

13. H. Bateman, *Partial Differential Equations of Mathematical Physics*, Cambridge University Press, Cambridge, England, 1932

14. I. N. Sneddon, *Elements of Partial Differential Equations*, McGraw-Hill, New York, 1957

15. T. Myint-U, *Partial Differential Equations for Scientists and Engineers*, North Holland, New York, 1987

16. J. Mathews, R. Walker, *Mathematical Methods of Physics*, 2nd Edition, Addison-Wesley Publishing Company, Redwood City, California, 1970

17. G. Arfken, *Mathematical Methods for Physicists*, 2nd Edition, Academic Press, Orlando Florida, 1985

18. M. Abramowitz, I. A. Stegun, *Handbook of Mathematical Functions*, National Bureau of Standards, 1972

19. C. V. Raman, K. S. Krishna, "A New Type of Secondary Radiation," Nature, 121, 501 (1928)

20. C. Cohen-Tannoudji, B. Diu, F. Laloe, *Quantum Mechanics*, John Wiley and Sons, New York, 1977

21. A. Yariv, Quantum Electronics, Second Edition, John Wiley and Sons, New York, 1975

22. Y. R. Shen, N. Bloembergen, "Theory of Stimulated Brillouin and Raman Scattering," Physical Review, 177, A1787 (1965)

23. J. A. Giordmaine, W. Kaiser, "Light Scattering by Coherently Driven Lattice Vibrations," Physical Review, 144, 676 (1966)

24. M. Maier, W. Kaiser, J. A. Giordmaine, "Backward Stimulated Raman Scattering,"

25. G. Placzek, *Marx Handbuch der Radiologie*, Academische Verlagsgesellschaft, Leipzig, 1934

26. J. Rifkin, M. Bernt, J. L. Carlsten, "Gain Enhancement in a XeCl-pumped Raman Amplifier," Journal of the Optical Society of America B, 5, 1607 (1988)

27. L. Allen, J. Eberly, *Optical Resonance and Two Level Atoms*, John Wiley and Sons, New York, 1975

28. M. G. Raymer, L. A. Westling, "Quantum Theory of Stokes Generation with Multimode Lasers," Journal of the Optical Society of America B, 2, 1417 (1985)

29. G. G. Lombardi, H. Injeyan, "Phase Correlation in a Raman Amplifier," Journal of the Optical Society of America B, 3, 1461 (1986)

30. Z. W. Li, C. Radzewicz, M. G. Raymer, "Phase Cross Correlation in the Coherent Raman Process," Optics Letters, 13, 491 (1988)

31. D. C. MacPherson, R. C. Swanson, J. L. Carlsten, "Quantum Fluctuations in the Stimulated-Raman Scattering Linewidth," Physical Review Letters, 61, 66 (1988)

32. M. D. Duncan, R. Mahon, L. L. Tankersley, J. Reintjes, "Transient Stimulated Raman Amplification in Hydrogen," Journal of the Optical Society of America B, 5, 37 (1988)

33. G. Herzberg, *Spectra of Diatomic Molecules*, Van Nostrand, Princeton, New Jersey, 1950

34. R. W. Minck, E. E. Hagenlocker, W. G. Rado, *Considerations and Evaluation of Factors Influencing the Stimulated Optical Scattering in Gases*, Report #SL66-24, Ford Motor Company

35. R. Eisberg, R. Resnick, *Quantum Physics of Atoms, Molecules, Solids, Nuclei, and Particles*, John Wiley and Sons, New York, 1974

36. H. Szymanski, Editor, *Raman Spectroscopy, Theory and Practice*, Plenum Press, New York, 1967

37. W. H. Miller, Editor, *Dynamics of Molecular Collisions, Part A*, Plenum Press, New York, 1976

APPENDICES

APPENDIX A

RIEMANNS METHOD

Introduction

In this appendix, Riemann's method for the solution of 2nd order, linear, hyperbolic, partial differential equations is presented. The motivations behind this appendix are due to the fact that Riemann's method is a powerful and elegant mathematical tool which is rather obscure. It is not commonly found in text books and does not appear to be widely used falling victim to more robust methods such as Laplace transforms. For these reasons, it seems appropriate to include it in this thesis.

Riemann's Method

Although obscure, Riemann's Method does appear in a number of texts[13,14,15]. The most complete presentation is that given by Myint-U[15] which shall be followed closely here. The method concerns itself with the integration of linear second order hyperbolic partial differential equations subject to Cauchy boundary conditions[16]. The solution, therefore, will be sought at a point $P(\alpha, \beta)$ in the plane of the normal coordinates x and y. The solution and one first order partial derivative must also be specified along a curve Λ in the x-y plane to stipulate the Cauchy boundary conditions, as shown in Figure 16.

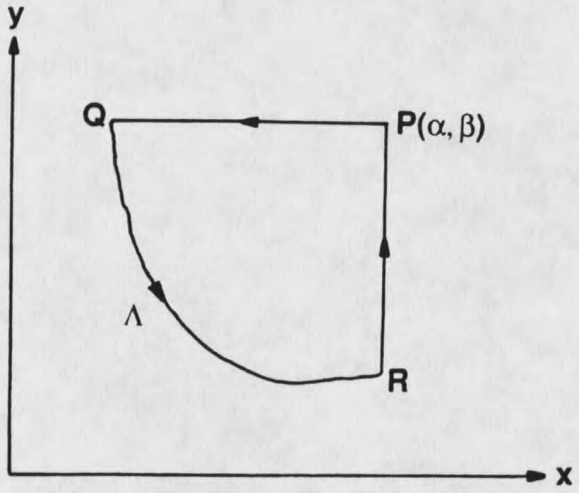


Figure 16. Contour used in developing generalized Riemann solution of hyperbolic partial differential equations. The solution is sought at P(α, β). X and Y denote the normal coordinates.

We begin by defining the most general linear second order hyperbolic PDE as an operator equation[16]

$$\hat{L}[u] = u_{xy} + a u_x + b u_y + c u = f(x, y) \qquad (A.1)$$

Here the coefficients a, b, and c can be functions of x and y and are assumed to be well behaved having continuous derivatives and no singularities in the region of interest. The subscripts denote partial derivatives. Further, in the spirit of Sturm-Liouville theory[17], we define the adjoint operator of $\hat{L}$ to be

$$\hat{M}[v] = v_{xy} - (av)_x - (bv)_y + cv \qquad (A.2)$$

as well as the functions

$$U = auv - uv_y \qquad (A.3)$$

and

$$V = buv - vu_x \tag{A.4}$$

where v is (for the moment) an arbitrary function of x and y. Appropriate algebraic manipulation shows that

$$v\hat{L}[u] - u\hat{M}[v] = U_x + V_y \tag{A.5}$$

Application of Greens' Theorem yields

$$\int_S (U_x + V_y)dxdy = \oint_C (Udx - Vdy)$$

C is a contour enclosing the surface S in the x-y plane. We assume that u and u_x are known for the contour shown in Figure 16. We have dy = 0 on PQ and dx = 0 on PR so that the contour integral may be broken up to yield

$$\int_S (v\hat{L}[u] - u\hat{M}v])\, dxdy = \int_Q^R (Udy - Vdx) + \int_R^P Udy - \int_P^Q Vdx \tag{A.6}$$

Substitution of (A.4) into the last term on the right side of (A.6) and integration by parts with respect to x gives

$$\int_P^Q Vdx = (uv)\Big|_P^Q + \int_P^Q u(bv - v_x)dx \tag{A.7}$$

Using (A.3) in the second integral on the right of (A.6), and (A.7) allows the entire expression to be written as

$$uv\Big|_P = uv\Big|_Q + \int_P^Q u(bv - v_x)dx - \int_R^P u(av - v_y)dy - \int_Q^R (Udy - Vdx) \tag{A.8}$$

This expression can be made tractable by demanding that $\hat{M}[v] = 0$ and

$$v_x = bv \text{ for } y = \beta \tag{A.9a}$$

$$v_y = av \text{ for } x = \alpha \tag{A.9b}$$

$$v = 1 \text{for} (x, y) = (\alpha, \beta) \qquad (A.9c)$$

The function v is now known as the Riemann-Green function. Invoking (A.9) we obtain the result

$$u \Big|_P = uv \Big|_Q - \int_Q^R vu(ady - bdx) + \int_Q^R (uv_y dy - vu_x dx) + \int_S vfdxdy \qquad (A.10)$$

Now, assume that u_y and not u_x is known along Λ. Similar considerations will yield the expression

$$u \Big|_P = uv \Big|_R - \int_Q^R vu(ady - bdx) + \int_Q^R (uv_x dx - vu_y dy) + \int_S vfdxdy \qquad (A.11)$$

Addition of (A.10) and (A.11) gives the general result

$$u \Big|_P = \frac{1}{2}\left(uv \Big|_Q + uv \Big|_R\right) - \int_Q^R uv(ady - bdx) - \frac{1}{2}\int_Q^R u(v_x dx - v_y dy) +$$

$$\frac{1}{2}\int_Q^R v(u_x dx - u_y dy) + \int_S vfdxdy \qquad (A.12)$$

Equation (A.12) is the general solution for the operator equation $\hat{L}[u] = f(x, y)$ with appropriate Cauchy boundary conditions along Λ. With clairvoyance we shall now adapt the solution (A.12) to a rectangular contour where u_y is known on the y-axis and u_x is known along the x-axis. Further we shall assume $f(x, y) = a = b = 0$. Considering the rectangular contour in Figure 17, equation (A.12) becomes

$$u \Big|_P = \frac{1}{2}\left(uv \Big|_Q + uv \Big|_R\right) - \frac{1}{2}\int_Q^R (vu_y - uv_y)dy + \frac{1}{2}\int_Q^R (vu_x - uvsuvx)dx \qquad (A.13)$$

We have dx = 0 on QA and dy = 0 on AR. The integrals are evaluated as follows

$$\frac{1}{2}\int_Q^R \left(v\frac{\partial u}{\partial y} - u\frac{\partial v}{\partial y}\right)dy = \frac{uv}{2}\Big|_Q + \int_A^Q v\frac{\partial u}{\partial y}dy \qquad (A.14a)$$

and

$$\frac{1}{2}\int_{Q}^{R}\left(v\frac{\partial u}{\partial x}-u\frac{\partial v}{\partial x}\right)dx=\left(\frac{uv}{2}\Big|_{R}-\frac{uv}{2}\Big|_{A}-\int_{A}^{R}u\frac{\partial v}{\partial x}dx \qquad (A.14b)$$

Substitution of (A.14) into (A.13) yields the result

$$u\Big|_{P}=uv\Big|_{R}-\int_{A}^{R}uv_{x}dx+\int_{A}^{Q}vu_{y}dy \qquad (A.15)$$

With (A.15) we are now in a position to apply this method to the Raman equations.

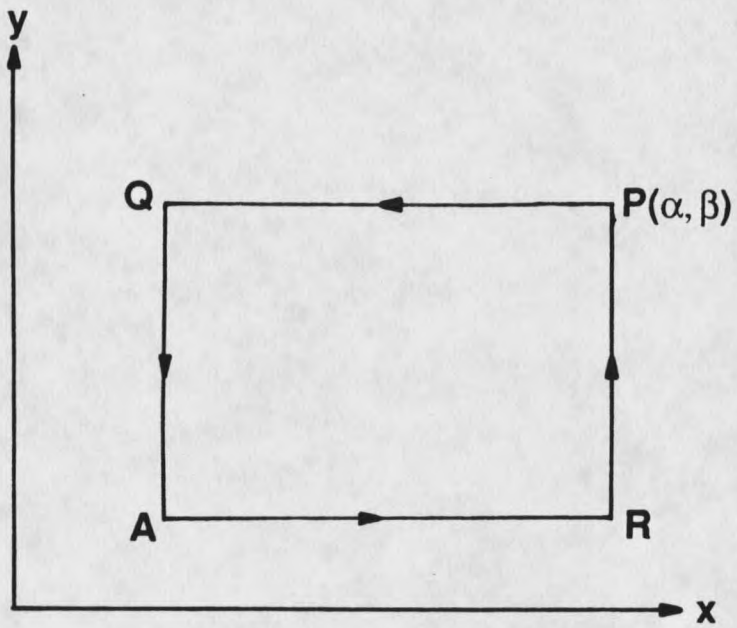


Figure 17. Contour used to adapt the generalized Riemann solution to the Raman equations.

APPENDIX B

COMPUTER PROGRAMS

Figure 18. Computer program GLATT.

```
**********************************************************************
PROGRAM GLATT
This program smooths data from a noisy source...typically the LP energy meter reading is
gain enhancement experiments. It uses the algorithms found in 'Numerical Recipes'.-
..SMOOFT (page 495), REALFT (page 400), and FOUR1 (page 394). This program
does not need to know the X coordinate of the data. The parameter PTS is a user
specified quantity related to the amount of smoothing desired. PTS=0 gives no smooth-
ing while PTS greater than half the number of total points renders the data featureless.
**********************************************************************
*
      IMPLICIT REAL*8 (A-H,O-Z)
      REAL*8 Y(1024), YNEW(1024)
      CHARACTER*20 FNAME
      CHARACTER*20 YNAME
5     FORMAT(A20)
*
      WRITE(*,*) 'INPUT THE NAME OF FILE TO BE SMOOTHED'
      READ(*,5) FNAME
      OPEN(UNIT = 1, FILE = FNAME, STATUS = 'OLD')
*
      WRITE(*,*) 'WHAT DO YOU WANT TO CALL THE OUTPUT FILE?'
      READ(*,5) YNAME
      OPEN(UNIT = 2, FILE = YNAME, STATUS = 'NEW')
*
      DO 10 I = 1 , 1024
          READ(1,*,END = 20) Y(I)
10    CONTINUE
20    WRITE(*,*) 'FILE   ',FNAME,' IS LOADED'
      N = I - 1
      WRITE(*,*)'THE VALUE OF N IS',N
*
      WRITE(*,*)'INPUT THE VALUE OF PTS'
      READ(*,*) PTS
*
      DO 100 J = 1 , N
*         WRITE(*,*)'THERE ARE  ',N-J,'  ITERATIONS LEFT'
          CALL SMOOFT(Y, N, PTS)
          YNEW(J) = Y(J)
          WRITE(2,*) YNEW(J)
100   CONTINUE
*
      CLOSE (UNIT = 1)
      WRITE(*,*)'YNEW ARRAY IS LOADED INTO  ',YNAME
      CLOSE (UNIT = 2, STATUS = 'KEEP')
      STOP
      END
*
                        END MAIN PROGRAM
**********************************************************************
```

Figure 18. Continued.

The subroutine SMOOFT along with the supporting subroutines REALFT and FOUR1 are to be found in reference 12 (Numerical Recipes) on pages 495, 400, and 394 respectively and therefore will not be given here.

Figure 19. Computer program LFELD.

```
**********************************************************************
PROGRAM 'LFELD' VERSION 3. MAR 30, 1989
This program computes the input laser field, start up Stokes field or fully correlated
Stokes field for stimulated Raman scattering. It is based on the fixed random phase
model for broadband lasers and calculates the fields by summing the fields produced by
the individual modes of the laser. The amplitudes of each mode are weighted by a
Lorentzian about the center of the mode structure.
The random number generator is taken from 'Numerical Recipes' (page 197). IDUM
must be set to a negative INTEGER to initialize the function RAN3.
Units implicit to this program are centimeters and nanoseconds. The conversion from
wavenumbers to frequency is via 2*pi*c. c (speed of light) is equal to 30 cm/ns in these
units.
Update: added scaling features. The pump energy is normalized to 1. The Stokes fields
are scaled to give a physically meaningful value. As a check, the corresponding energy
integral is calculated.
**********************************************************************
*
      IMPLICIT REAL*8 (A-H,O-Z)
      IMPLICIT INTEGER*4 (I - N)
      REAL*8 PHIL(750), PHIS(750), AMPL(750), P(500)
      REAL*8 ZL(500), ZS(500), AREA(500), AMPS(759), TYME(500)
      COMPLEX*8 EL(500), ES(500)
      COMPLEX*8 LASER, STOKES
*
      PI = 3.1415926
      C = 30.
*
1     FORMAT (A20)
500   FORMAT (F10.6,2X,F12.8)
*
      WRITE(*,*)'WHAT IS THE NUMBER OF MODES?'
      READ(*,*) MODES
      WRITE(*,*)'WHAT IS THE MODE SPACING IN cm-1?'
      READ(*,*) DELTA
      WRITE(*,*)'WHAT IS THE PULSE LENGTH IN ns?'
      READ(*,*) TMAX
      WRITE(*,*)'WHAT IS THE NUMBER OF INTERVALS IN THE PULSE?'
      READ(*,*) INTRVAL
      WRITE(*,*)'WHAT IS THE HALFWIDTH OF THE LORENTZIAN IN
cm-1?'
      READ(*,*) HWIDTH
      WRITE(*,*)'WHAT IS THE STOKES FIELD SCALE FACTOR?'
      READ(*,*) ESSCALE
      WRITE(*,*)'INPUT A NEGATIVE INTEGER FOR RANDOM SEED'
      READ(*,*) IDUM
      OPEN(UNIT = 1,FILE = 'PARAMS.DAT', STATUS = 'NEW')
      WRITE(1,*) INTRVAL, TMAX
      CLOSE(UNIT = 1)
```

Figure 19. Continued.

```
      IMAX = INTRVAL + 1
*
      WRITE(*,*)'CALCULATING RANDOM PHASES.....'
      DO 100 I = 1, MODES
            RANDUM = RAN2(IDUM)
            PHIL(I) = 2*PI*RANDUM
            PHIS(I) = PHIL(I)
100   CONTINUE
*
      DELTA = 2 * PI * C * DELTA
      HWIDTH = 2 * PI * C * HWIDTH
      J0 = MODES/2
      ASUM = 0.
*
      WRITE(*,*)'CALCULATING WEIGHTED AMPLITUDES.....'
      DO 150 J = 1,MODES
            AMPL(J) = 1./(HWIDTH**2 + (DELTA*(J0-J))**2)
            ASUM =ASUM + AMPL(J)
150   CONTINUE
*
      SCALE = 1./DSQRT(ASUM)
*
      DO 175 J = 1,MODES
            AMPL(J) = SCALE*DSQRT(AMPL(J))
            AMPS(J) = AMPL(J)
175   CONTINUE
*
      WRITE(*,*)'CALCULATING THE LASER AND STOKES FIELDS.....'
      OPEN(UNIT=2,FILE='PMPFELD.DAT',STATUS='NEW')
      OPEN(UNIT=3,FILE='STKFELD.DAT',STATUS='NEW')
      TSTEP = TMAX/INTRVAL
      T = 0.
      DO 200 I = 1,INTRVAL
            CALL FIELD(AMPL,AMPS,PHIL,PHIS,DELTA,
     C    MODES,T,LASER,STOKES)
            EL(I) = LASER
            ZL(I) = EL(I)*CONJG(EL(I))
            ES(I) = STOKES
            ZS(I) = ES(I)*CONJG(ES(I))
            T = T + TSTEP
200   CONTINUE
*
      WRITE(*,*)'CALCULATING THE ENERGY INTEGRAL p(t).....'
      OPEN(UNIT=4,FILE='ERGPUMP.DAT',STATUS='NEW')
      SUM = 0.
      T = 0.
      AREA(1) = ZL(1) * TSTEP/2.
      SUM = AREA(1)
      P(1) = SUM
```

Figure 19. Continued.

```
            TYME(1) = T
            T = TSTEP
            WRITE(4,500) TYME(1), P(1)
*
            DO 225 J = 2,IMAX
                  AREA(J) = (ZL(J) + ZL(J-1))*TSTEP/2.
                  SUM = AREA(J) + SUM
                  P(J) = SUM
                  TYME(J) = T
                  T = T + TSTEP
 225        CONTINUE
            WRITE(*,*)'The value of the integral is ',SUM
            WRITE(*,*)'Normalizing energy and fields.....'
            ZSCALE = 1./P(IMAX)
            DO 250 J = 1,IMAX
                  P(J) = ZSCALE*P(J)
                  WRITE(4,500) TYME(J), P(J)
 250        CONTINUE
            CLOSE(UNIT=4)
*
C           open(unit=6,file='intens.dat',status='new')
            DO 275 K = 1,INTRVAL
                  EL(K) = DSQRT(ZSCALE)*EL(K)
                  ES(K) = ESSCALE*DSQRT(ZSCALE)*ES(K)
                  WRITE(2,*) EL(K)
                  WRITE(3,*) ES(K)
C                 biff=conjg(el(k))*el(k)
C                 boff=conjg(es(k))*es(k)
C                 write(6,*) tyme(k),biff,boff
 275        CONTINUE
*
            SUMS = 0.
            AREAS = ES(1)*CONJG(ES(1))*TSTEP/2.
            SUMS = AREAS
            DO 300 KK=1,IMAX
                  AREAS = (ES(KK)*CONJG(ES(KK)) + ES(KK-1)*CONJG(ES(KK-1)))
   C              *TSTEP/2.
                  SUMS = AREAS + SUMS
 300        CONTINUE
            write(*,*)'sums = ',sums
            DLAMBDA = 7.5068D-10*SUMS
            WRITE(*,*)'The Stokes energy is ', DLAMBDA,'Joules'
*
            CLOSE(UNIT=2)
            CLOSE(UNIT=3)
C           close(unit=6)
*
            STOP
            END
```

Figure 19. Continued.

```
      FUNCTION RAN2(IDUM)
      IMPLICIT REAL*8 (A-H,O-Z)
      IMPLICIT INTEGER*4 (I-N)
      REAL*8 IR(97)
      PARAMETER (M=714025, IA=1366, IC=150899)
      DATA IFF /0/
*
      RM = 1./M
      IF (IDUM .LT. 0 .OR. IFF .EQ.0) THEN
          IFF = 1
          IDUM = MOD(IC-IDUM,M)
          DO 11 J =1,97
              IDUM = MOD(IA*IDUM+IC,M)
              IR(J) = IDUM
11        CONTINUE
          IDUM = MOD(IA*IDUM+IC,M)
          IY = IDUM
      ENDIF
      J = 1 + (97*IY)/M
      IF (J .GT. 97 .OR. J .LT.1) PAUSE
      IY = IR(J)
      RAN2 = IY*RM
      IDUM = MOD(IA*IDUM + IC,M)
      IR(J) = IDUM
      RETURN
      END
*
*
                        SUBROUTINE FIELD
*************************************************************************

  SUBROUTINE FIELD(AMPL,AMPS,PHIL,PHIS,
C     DELTA,MODES,T,LASER,STOKES)
      IMPLICIT REAL*8(A-H,O-Z)
      COMPLEX LASER, STOKES
      REAL*8 AMPL(750), AMPS(750), PHIL(750), PHIS(750)
*
      ELR = 0.
      ELI = 0.
      ESR = 0.
      ESI = 0.

*
      DO 1 M = 1,MODES
          OMEGAT = DELTA * M * T
          UL = OMEGAT + PHIL(M)
          ELR = ELR + AMPL(M)*COS(UL)
```

Figure 19. Continued.

```
                ELI + ELI + AMPL(M)*SIN(UL)
*
                US = OMEGAT + PHIS(M)
                ESR = ESR + AMPS(M)*COS(US)
                ESI = ESI + AMPS(M)*SIN(US)
*
 1        CONTINUE
          LASER = CMPLX(ELR,ELI)
          STOKES = CMPLX(ESR,ESI)
*
          RETURN
          END
```

Figure 20. Computer program RAMAN.

```
************************************************************************
PROGRAM RAMAN.FOR  VERSION 4  MARCH 31, 1989
This program calculates the analytic integral for the transient Raman equations for no
pump depletion.
Update:  Version 4 has scaling features which will give the output in real quantities.  The
output will be given in Joules for both pump and Stokes.
GAMMAR is given in nanoHz & K1K2 in m/(V**2 s)
W0 is the beam waist in square meters
EPSILON is permattivity constant & Cvel is the speed of light
************************************************************************
*
      IMPLICIT REAL*8(A-H,O-Z)
      REAL*8 P(500),TIME(500),F(500),ESINTEN(500)
      REAL*8 K1K2
      COMPLEX*8 EL(500),ES(500),ESTOKES(500),ZS(500)
      COMMON GAMMAR
      PI = 3.1415927
      W0 = 3.0D-4
      EPSILON = 8.85D-12
      CVEL = 2.99792D8
      Z = 1.D0
*
      OPEN(UNIT=1,FILE='PARAMS.DAT',STATUS='OLD')
      READ(1,*) INTRVAL,TMAX
      CLOSE(UNIT=1)
      TSTEP = TMAX/INTRVAL
      WRITE(*,*)'Intrval Tmax and Tstep are '
      WRITE(*,*) INTRVAL,TMAX,TSTEP
      WRITE(*,*)'  '
      OPEN(UNIT=2,FILE='ERGPUMP.DAT',STATUS='OLD')
      OPEN(UNIT=3,FILE='PMPFELD.DAT',STATUS='OLD')
      OPEN(UNIT=4,FILE='STKFELD.DAT',STATUS='OLD')
*
      DO 10 I=1,500
          READ(2,*,END=11) TIME(I),P(I)
10    CONTINUE
11    DO 12 I=1,500
          READ(3,*,END=13) EL(I)
12    CONTINUE
13    DO 14 I=1,500
          READ(4,*,END=15) ES(I)
14    CONTINUE
15    WRITE(*,*)'ERGPUMP PMPFELD and STKFELD files loaded.....'
      CLOSE(UNIT=2)
      CLOSE(UNIT=3)
      CLOSE(UNIT=4)
```

Figure 20. Continued.

```
C       OPEN(UNIT=5,FILE='SFIELD.DAT',STATUS='NEW')
        OPEN(UNIT=6,FILE='ESOUT.DAT',STATUS='NEW')
*
        IMAX = I - 1
        WRITE(*,*)'IMAX = ',IMAX
        WRITE(*,*)'Input Gmin Gmax and number of intervals.....'
        READ(*,*)'GMIN,GMAX,INTVALG
        WRITE(*,*)'Choose 10 or 100 atmospheres,,,input 10 or 100'
        READ(*,*) PRESS
        IF(PRESS .EQ. 10) THEN
            GAMMAR = 1.532
            K1K2 = 6.68D-5
            CMIN = DSQRT(GMIN*GAMMAR/2.)
            CMAX = DSQRT(GMAX*GAMMAR/2.)
            WRITE(*,*)'10 atmospheres was chosen...Gamma =',GAMMAR
            WRITE(*,*)'Calculated values for Cmin and Cmax are'
            WRITE(*,*) CMIN,CMAX
        ENDIF
        CSTEP = (CMAX - CMIN)/INTVALG
        WRITE(*,*)'The stepsize for C is ',CSTEP
        CAIN = CMIN
C       write(*,*)'input the gain'
C       read(*,*) gain
        DO 100 K = 1,INTVALG
            WRITE(*,*)'THE VALUE OF C IS ',CAIN
            T = 0.
            ESTOKES(1) = CMPLX(0.,0.)
            ESINTEN(1) = CONJG(ESTOKES(1))*ESTOKES(1)
C           WRITE(5,*) T,ESINTENS(1)
            T = TSTEP
            TPRIME = 0.
            NTPRIME = 0
*
c calculating the array of integrands
*
            DO 20 NT = 1,IMAX
                IF(NT .EQ. 1) THEN
                    CALL INTGRAT(P,EL,ES,T,TPRIME,NT,
  C                 NTPRIME,CAIN,GRAND)
                    F(1) = GRAND
                ENDIF
                DO 25 NTPRIME = 1,NT-1
                    CALL INTGRAT(P,EL,ES,T,TPRIME,NT,
  C                 NTPRIME,CAIN,GRAND)
                    F(NTPRIME) = GRAND
                    TPRIME = TPRIME + TSTEP
25              CONTINUE
```

Figure 20. Continued.

```
c doing the summation to get the intergal for specific t
*
                    SUM = 0.
                    AREA = F(1)*TSTEP/2.
                    SUM = AREA
                    DO 30 J = 2,NT
                        AREA = (F(J-1) + F(J))*TSTEP/2.
                        SUM = SUM + AREA
 30                 CONTINUE
*
c calculation of Es(z t) and the energy integral
*
                    ESTOKES(NT+1) = ES(NT+1) + CAIN*EL(NT+1)*SUM
                    ESINTEN(NT+1) = CONJG(ESTOKES(NT+1))*
    C               ESTOKES(NT+1)
C                   WRITE(5,*) T, ESINTEN(NT+1)
                    T = T + TSTEP
                    TPRIME = 0.
                    DO 31 KOUNT = 1,NT
                        F(KOUNT) = 0.
 31                 CONTINUE
*
 20             CONTINUE
*
                SUM1 = 0.
                AREA1 = ESINTEN(1)*TSTEP/2.
                SUM1 = AREA1
                DO 35 JJ = 2,NT+1
                    AREA1 = (ESINTEN(JJ) + ESINTEN(JJ-1))*TSTEP/2.
                    SUM1 = SUM1 + AREA1
 35             CONTINUE
                ENERGYS = EPSILON*CVEL*PI*(W0**2)*SUM1
                WRITE(*,*)'The Stokes Energy is ',ENERGYS,' Joules'
                ENERGYS = 1.0D6 * ENERGYS
                ERGSLOG = DLOG10(ENERGYS)
*
                ENERGYP = EPSILON*CVEL*PI*(W0**2)*(CAIN**2)/(K1K2*Z)
                WRITE(*,*)'The Pump Energy is ',ENERGYP,' Joules'
                ENERGYP = 1.0D3 * ENERGYP
*
                WRITE(6,*) ENERGYP,ERGSLOG
*
                CAIN = CAIN + CSTEP
 100        CONTINUE
C           CLOSE(UNIT=5)
            CLOSE(UNIT=6)
*
```

Figure 20. Continued.

```
      STOP
      END

                        END MAIN PROGRAM
*****************************************************************************
      SUBROUTINE INTGRAT(P,EL,ES,T,TPRIME,NT,
     C  NTPRIME,CAIN,GRAND)
      IMPLICIT REAL *8(A-H,O-Z)
      REAL*8 P(500)
      COMPLEX*8 EL(500), ES(500)
      COMMON GAMMAR
      IF(NTPRIME .EQ. 0) THEN
           DELP = P(NT)
           PIECE1 = CONJG(EL(1))*ES(1)/DSQRT(DELP)
      ELSE
           DELP = P(NT) - P(NTPRIME)
           PIECE1 = CONJG(EL(NTPRIME))*ES(NTPRIME)/DSQRT(DELP)
      ENDIF
      X = 2.*CAIN*DSQRT(DELP)
      BESSEL = BESSI1(X)
      PIECE2 = DEXP(-GAMMAR*(T - TPRIME))
      GRAND = PIECE1*PIECE2*BESSEL
      RETURN
      END
*****************************************************************************
*
      FUNCTION BESSI1(X)
*
      IMPLICIT REAL*8(A-H,O-Z)
      REAL*8 Y,P1,P2,P3,P4,P5,P6,P7
      REAL*8 Q1,Q2,Q3,Q4,Q5,Q6,Q7,Q8,Q9
      DATA P1,P2,P3,P4,P5,P6,P7/0.5D0,0.87890594D0,0.51498869D0,
     *     0.15084934D0,0.2658733D-1,0,301532D-2,0.32411D-3/
      DATA Q1,Q2,Q3,Q4,Q5,Q6,Q7,Q8,Q9,/0.39894228D0,-0.3988024D-1,
     *     -0.362018D-2,0.163801D-2,-0.1031555D-1,0.2282967D-1,
     *     -0.2895312D-1,0.1787654D-1,-0.420059-2/
*
      IF(DABS(X) .LT. 3.75) THEN
           Y = (X/3.75)**2
           BESSI1 = X*(P1+Y*(P2+Y*(P3+Y*(P4+Y*(P5+Y*(P6+Y*P7))))))
      ELSE
           AX = DABS(X)
           Y = 3.75/AX
           BESSI1 = (DEXP(AX)/DSQRT(AX))*(Q1+Y*(Q2+Y*(Q3+Y*
     C          (Q4+Y*(Q5+Y*(Q6+Y*(Q7+Y*(Q8+Y*Q9))))))))
      ENDIF
      RETURN
      END
```

Figure 21. Computer program AVEFILE.

```
**********************************************************************
PROGRAM AVEFILE  MAY 12, 1989
This program averages the y values of four data files.  It is necessary to load the x and y
values into arrays.  The x values need not be equally spaced.  The routine RATINT (Nu-
merical Recipes p. 85) will interpolate for the values of y at x values which the program
generates.
**********************************************************************
*
      IMPLICIT REAL*8(A-H,O-Z)
      PARAMETER (NSIZE=256)
      REAL*8 X1DAT(NSIZE),X2DAT(NSIZE)
      REAL*8 X3DAT(NSIZE),X4DAT(NSIZED),
     C  Y1DAT(NSIZE),Y2DAT(NSIZE),Y3DAT(NSIZE),Y4DAT(NSIZE),
     C  XOUT(NSIZE),YOUT(NSIZE0
      CHARACTER*(20) FONE,FTWO,FTHREE,FFOUR,FOUT
1     FORMAT(A20)
      WRITE(*,*)'Input the files to be averaged.'
      READ(*,1) FONE
      READ(*,1) FTWO
      READ(*,1) FTHREE
      READ(*,1) FFOUR
      WRITE(*,*)'Name of the output file? '
      READ(*,1) FOUT
      OPEN(UNIT = 1, FILE = FONE, STATUS = 'OLD')
      OPEN(UNIT = 2, FILE = FTWO, STATUS = 'OLD')
      OPEN(UNIT = 3, FILE = FTHREE, STATUS = 'OLD')
      OPEN(UNIT = 4, FILE = FFOUR, STATUS = 'OLD')
      OPEN(UNIT = 5, FILE = FOUT, STATUS = 'NEW')
      DO 11 I = 1,NSIZE
          READ(1,*,END = 12) X1DAT(I),Y1DAT(I)
11    CONTINUE
12    X1MAX = X1DAT(I-1)
      I1MAX = I-1
      DO 13 I = 1,NSIZE
          READ(2,*,END = 14) X2DAT(I),Y2DAT(I)
13    CONTINUE
14    X2MAX = X2DAT(I-1)
      I2MAX = I-1
      DO 15 I = 1,NSIZE
          READ(3,*,END = 16) X3DAT(I),Y3DAT(I)
15    CONTINUE
16    X3MAX = X3DAT(I-1)
      I3MAX = I-1
      DO 17 I = 1,NSIZE
          READ(4,*,END = 18) X4DAT(I),Y4DAT(I)
17    CONTINUE
18    X4MAX = X4DAT(I-1)
      I4MAX = I-1
```

Figure 21. Continued.

```
      WRITE(*,*)' Input files read.....'
      WRITE(*,*)'Xmax value are'
      WRITE(*,*) X1MAX, X2MAX, X3MAX, X4MAX
      WRITE(*,*) ' '
      WRITE(*,*)'Imax values are.....'
      WRITE(*,*) I1MAX,I2MAX,I3MAX,I4MAX
      WRITE(*,*)'Input XMIN XMAX and INTX values. '
      READ(*,*) XMIN, XMAX, INTX
      DELX = (XMAX - XMIN)/INTX
      X=XMIN
*
      DO 50 J = 1,INTX+1
            CALL RATINT(X1DAT,Y1DAT,I1MAX,X,Y1,DY)
            CALL RATINT(X2DAT,Y2DAT,I2MAX,X,Y2,DY)
            CALL RATINT(X3DAT,Y3DAT,I3MAX,X,Y3,DY)
            CALL RATINT(X4DAT,Y4DAT,I4MAX,X,Y4,DY)
            XOUT(J) = X
            YOUT(J) = (Y1+Y2+Y3+Y4)/4.
            WRITE(5,*) XOUT(J),YOUT(J)
            X = X +DELX
50    CONTINUE
      CLOSE(UNIT = 1)
      CLOSE(UNIT = 2)
      CLOSE(UNIT = 3)
      CLOSE(UNIT = 4)
      STOP
      END

      SUBROUTINE RATINT(XA,YA,N,X,Y,DY)
      IMPLICIT REAL*8(A-H,O-Z)
      PARAMETER (NMAX = 256, TINY = 1.D-25)
      REAL*8 XA(N),YA(N),C(NMAX),D(NMAX)
*
      NS =1
      HH = DABS(X-XA(1))
      DO 11 I =1,N
            H = DABS(X-XA(I))
            IF (H.EQ.0) THEN
                  Y = YA(I)
                  DY = 0.D0
                  RETURN
            ELSE IF (H.LT.HH) THEN
                  NS = I
                  HH = H
            ENDF
            C(I) = YA(I)
```

Figure 21. Continued.

```
            D(I) = YA(I) + TINY
 11       CONTINUE
*
          Y = YA(NS)
          NS = NS-1
*
          DO 13 M = 1,N-1
               DO 12 I = 1,N-M
                    W = C(I+1) - D(I)
                    H = XA(I+M) - X
                    T = (XA(I)-X)*D(I)/H
                    DD = T - C(I+1)
                    IF (DD.EQ.0.D0) PAUSE
                    DD = W/DD
                    D(I) = C(I+1)*DD
                    C(I) = T*DD
 12            CONTINUE
          IF (2*NS.LT.N-M) THEN
               DY = C(NS+1)
          ELSE
               DY = D(NS)
               NS = NS-1
          ENDIF
          Y = Y+DY
 13       CONTINUE
*
          RETURN
          END
```

Figure 22. Computer program DEVIATION.

```
**********************************************************************
PROGRAM 'DEVIATION' VERSION 2  MAY 23, 1989
This program calculates the standard deviations for the averaged data files from the
RAMAN4 program.  It uses rational interpolation to calculate deviations from the aver-
age curve at points which do not lie at the same x value as the average curve.  It uses
some novel code (impetus from Rand Swanson) to open only one file at a time.
Basically, this is a nested DO loop type structure.
**********************************************************************
*
      IMPLICIT REAL*8 (A-H,O-Z)
      PARAMETER (NSIZE = 512)
      REAL*8 XAVE(NSIZE), YAVE(NSIZE)
      REAL*8 DELSQR(NSIZE),YYOUT(NSIZE)
      REAL*8 XDAT(NSIZE), YDAT(NSIZE), DEVIATE(NSIZE)
      CHARACTER*(11) AVENAME, FNAME, OUTNAME
      CHARACTER*(3) PRE
      CHARACTER*(4) SUF
      CHARACTER*(2) ZNUMB
4     FORMAT (F9.6,2X,F9.6,2X,F9.6,2X,F9.6,2X,F9.6)
5     FORMAT (A11)
6     FORMAT (F9.6,2X,F9.6,2X,F9.6)
*
      WRITE(*,*)'Input the name of the averaged file.....'
      READ(*,5) AVENAME
      OPEN(UNIT = 1, FILE = AVENAME, STATUS = 'OLD')
      DO 11 I = 1,NSIZE
          READ(1,*,END12) XAVE(I), YAVE(I)
11    CONTINUE
12    IMAX = I-1
      WRITE(*,*)'IMAX = ',IMAX
      WRITE(*,*)'Averaged file loaded.....'
      CLOSE (UNIT = 1)
      WRITE(*,*)'What is the name of the output file? '
      READ(*,5) OUTNAME
      OPEN(UNIT = 3, FILE = OUTNAME, STATUS = 'NEW')
      WRITE(*,*)'what is the number of curves? '
      READ(*,*) NCURVES
      DO 13 J = 1,IMAX
          DELSQR(J) = 0.D0
13    CONTINUE
*
      WRITE(*,*)'What is the data..10 or 100 atm? '
      READ(*,*) PRESS
      IF (PRESS.EQ.10) THEN
          PRE = 'CEE'
          WRITE(*,*)'File prefix is CEE...'
      ENDIF
      IF (PRESS.EQ.100) THEN
```

Figure 22. Continued.

```
            PRE = 'BEE'
          WRITE(*,*)'File prefix is BEE...'
          ENDIF
          SUF = '.DAT'
*
          XMIN = XAVE(1)
          XMAX = XAVE(IMAX)
          WRITE(*,*)'Number of X intervals? '
          READ(*,*) INTX
          DELX = (XMAX - XMIN)/INTX
          WRITE(*,*)'Xmin Xmax and DelX are'
          WRITE(*,6) XMIN,XMAX,DELX
*
          DO 100 N = 1,NCURVES
               WRITE(*,*)'N = ',N
               M = N + 64
               ZNUMB = CHAR(M)
               FNAME = PRE//ZNUMB//SUF
               WRITE(*,*) FNAME
               OPEN(UNIT = 2, FILE = FNAME, STATUS = 'OLD')
*
          DO 20 L = 1,IMAX
               READ(2,*,END = 50) XDAT(L), YDAT(L)
 20       CONTINUE
 50       CLOSE(UNIT = 2)
          LMAX = L-1
          WRITE(*,*)'LMAX = ',LMAX
          X = XMIN
          DO 21 J = 1,INTX
               CALL RATINT(XDAT,YDAT,LMAX,X,Y,DY)
               CALL RATINT(XAVE,YAVE,IMAX,X,YY,DY)
               YYOUT(J) = YY
               DELSQR(J) = (Y - YY)**2 + DELSQR(J)
               X = X + DELX
 21       CONTINUE
*
 100      CONTINUE
*
          X = XMIN
          DO 101 J =1,INTX
               DEVIATE(J) = DSQRT((1/(NCURVES-1))*DELSQR(J))
               WRITE(3,4) X,YYOUT(J),YYOUT(J)+DEVIATE(J),
     C         YYOUT(J) - DEVIATE(J), DEVIATE(J)
               X = X + DELX
 101      CONTINUE
```

Figure 22. Continued.

```
*
      CLOSE(UNIT=3)
      WRITE(*,*)'Dats all you waskaly wabbit.....'
      STOP
      END
```

For subroutine RATINT source listing, see program AVEFILE2 above or on page 85 of Numerical Recipes[12].

APPENDIX C

CHARACTERIZATION OF MOLECULAR HYDROGEN AS A RAMAN SCATTERING MEDIUM

Introduction

Molecular hydrogen was the medium of choice in this thesis because it has the highest Raman gain of the readily available diatomic gases (e.g. H_2, N_2, O_2)[34]. In this appendix the characteristics of molecular hydrogen (H_2) as a Raman scattering medium are discussed. To obtain a physical picture it is necessary to use a spectroscopic viewpoint. For brevity, only the most simplistic models will be considered in this discussion. The fact that these models yield results very close to measured values justifies their use.

The hydrogen molecule can be excited in three energy regimes corresponding to electronic, vibrational, and rotational transitions. In exciting the gas with the 308 nm pump photon it is expected that neither normal electronic excitation nor electronic Raman scattering will occur. The reason for this is that the pump photon possesses only approximately one third the energy (32000 cm^{-1}) required to induce an excitation from the electronic ground state, which is the most populated at room temperature, to the first excited state (92000 cm^{-1}). This is not to say that the electronic states play no role in Raman scattering. Indeed, the virtual level to which the medium is driven by the pump photon is considered to be a superposition of electronic states, and it is the electronic states, or rather the detuning from resonance between the electronic states which determines to a large degree the polarizability of the molecule. As will be seen it is this quantity which leads to both vibrational and rotational Raman scattering. Because no true electronic transitions occur in this work it is necessary only to consider vibrational and rotational Raman scattering. To that end, the simple harmonic oscillator model will be used to explain vibrational Raman scattering, while the rigid rotator model is applied to the rotational Raman scattering. Further, only dipole interactions between the media and fields

will be considered because the transition probability for a dipole interaction dominates over other possible interactions (e.g.scattering from quadrupole or magnetic moments) by many orders of magnitude[33]. Thus the one dimensional scattering matrix elements of importance have the form[33]

$$P^{mn} = \int \psi_m^* P \psi_n \, dx \qquad (C.1)$$

Here P is the induced dipole moment or equivalently the polarization, and ψ denotes the time independent wave function. The integral is taken over all space. The importance of this assumption is manifested in the form of the selection rules for each Raman process, which arise from appropriate evaluation of (C.1). As extensive mathematical forays are not in the scope of this appendix, detailed derivation of the selection rules will not be undertaken. Rather, only semiquantitative explanations will be used where needed to make a point. The interested reader is referred to the cited literature for detailed calculations and proofs.

Vibrational Spectra

Application of the simple harmonic oscillator model to vibrational excitation can be justified as long as the potential well is not too anharmonic in the region of interest. Typically this is a good assumption for states with low energies. Assuming the validity of such an assumption, the energy of a level is given by the well known expression[33]

$$E_v = h\nu_0(v + 1/2), v = 0, 1, 2, \ldots \qquad (C.2)$$

The associated eigenfunctions are of the form

$$\psi_v = N_v e^{-\frac{1}{2}\beta x^2} H_v(\sqrt{\beta}x) \qquad (C.3)$$

Here, N_v is a normalization constant, x denotes the internuclear separation $\beta = 4\pi^2 m \nu_0 / h$, and $H_v(\sqrt{\beta}x)$ is the Hermite polynomial of order v. To obtain the selection rule for vibrational Raman transitions it is necessary to introduce some theory. It is known that homonuclear diatomic molecules exhibit no intrinsic vibrational spectrum[20,33,35]. This is because they lack a permanent electric dipole moment needed to couple adjacent vibrational states. Consequently, to obtain a vibrational Raman spectrum it is necessary to induce a dipole moment (i.e. a polarization in the electron cloud) in the molecule. This can be done by applying an electric (pump) field. Classically, it can be assumed that the dipole moment is directly proportional to the applied field, that is to say

$$P_i = \alpha_{ij} E_j,\ i,j = x,y,z \qquad (C.4)$$

α is known as the polarizability and is a tensor quantity. Intuitively it can be seen that a homonuclear diatomic molecule is more readily polarizable in one direction (e.g. along the internuclear axis) than in another. For such a case the polarization vector and the electric field will not in general be parallel so that α cannot be a simple constant of proportionality. In general α_{ij} consists of nine components, but by symmetry it can be shown[36] that $\alpha_\chi = \alpha_{ij}$ thereby reducing the number of unique components to six. Judicious choice of the molecular coordinate system can simplify the picture somewhat. If the electric field is chosen to be parallel to one of the molecules' axes of symmetry the components of (C.4) may be written as

$$P_i = \alpha_{ii} E_i,\ i = x,y,z \qquad (C.5)$$

Further, if the z axis is chosen to lie along the internuclear axis, then by symmetry $\alpha_{xx} = \alpha_{yy}$. To obtain the selection rule for vibrational Raman scattering the matrix element $P^{v v'}$ must be evaluated, and therefore knowledge of the explicit dependence of α on x is essential. It can be assumed as a first approximation that the polarizability varies

linearly with the internuclear separation x. The describing equation in one dimension is[1,21,22,23,24,25,32,33,36]

$$\alpha = \alpha_0 + \alpha' x \qquad (C.6)$$

where $\alpha' = (\partial\alpha/\partial x)_0$. The zero subscript denotes evaluation of the derivative about the equilibrium position. Substituting this result and (C.4) into the scattering matrix element (C.1) yields

$$P^{vv'} = |E|\alpha_0 \int \psi_v^* \psi_{v'} dx + |E|\alpha' \int \psi_v^* x \, \psi_{v'} dx \qquad (C.7)$$

Note that the integration is over the internuclear separation. Owing to the orthogonality properties of the Hemite polynomials of the eigenfunctions the first integral is zero except for $v = v'$, and leads only to Rayleigh scattering, while the second integral is non-zero only for the cases where $v = v' \pm 1$. This leads immediately to the selection rule $\Delta v = \pm 1$ for vibrational scattering. Under this selection rule the energy differences associated with the transitions are equally spaced and equal to $\Delta E_v = h\nu_0$. For molecular hydrogen ν_0 has a value of 1.24×10^{14} Hz [34] which yields a value of 0.514 eV for ΔE_v. As a result the Stokes emission arising from the 308 nm pump photon will have an expected energy of 3.51 eV and a corresponding wavelength of 353 nm. As can be seen, this value agrees to 0.5% of the value for Stokes emission (351 nm) given in the main body of this thesis, and provides ample justification for use of the simple harmonic oscillator model. For more accuracy, however, appropriate corrections must be added to the harmonic oscillator and rigid rotator models. Such corrections include the so-called nonrigid rotator, vibrating rotator, and symmetric top models[33,36]. For this work, however, the corrections are small and will not be considered. Thus it is clear that the Raman scattering seen in this work is vibrational in origin. Because the v = 0 level is most populated at room temperature, the majority of scattering is between the v = 0 and v = 1 states. To conserve energy it is necessary for the excited atoms to return from the v = 1 to the v = 0

state by some mechanism after the emission of the Stokes photon. This cannot be done by direct emission of a photon because such a transition is not allowed for diatomic homonuclear molecules. As mentioned earlier, this is due to the absence of a permanent electric dipole moment in such molecules which is needed to couple adjacent vibrational states. One manner in which the excited molecules return to the v = 0 state is known as V-T relaxation[37]. In this process the vibrational deexcitation occurs at the expense of increasing the translational kinetic energy of molecules during collisions, with the excess energy eventually going to heat the medium. The probability P_{10} for transitions between the v = 1 and v = 0 vibrational states can be calculated in a semiclassical manner using time dependent perturbation theory and the Morse potential for molecular interactions[37]. That such transitions are possible can be understood from a pedagodic viewpoint by arguments involving the Fourier transform of the interaction time, which provides a characteristic frequency spectrum of the collision event. If a component of this frequency spectrum overlaps strongly with the frequency of the corresponding forbidden transition the relaxation can occur.

Rotational Spectra

In the analysis of rotational spectra the traditional starting point is the rigid rotator model. In this model the diatomic molecule is replaced by its equivalent one body counterpart through the center of mass: $\mu = m_1 m_2/(m_1 + m_2)$. For molecular hydrogen the reduced mass is just the one half of the mass of a constituent proton. The quantum mechanical energy associated with a particular rotational state is given by[35]

$$E_j = \frac{\hbar^2}{2I} j(j+1), j = 0, 1, 2, \ldots \qquad (C.8)$$

Here, I is the moment of inertia of the molecule and can be taken to be μR_0^2, where R_0 is the equilibrium separation between the two atoms. The eigenfunctions for the rigid rotator are known as the so called *surface harmonics*[33] and have the form

$$\psi_j = N_j P_j^{|m|}(\cos\theta)\, e^{im\phi} \qquad (C.9)$$

Here N_j is an appropriate normalization factor, m is the standard azimuthal quantum number, ϕ and θ are the standard azimuthal and elevation angles of a spherical coordinate system respectively, and $P_j^{|m|}$ denotes the associated Legendre polynomial with argument $\cos\theta$.

The selection rule for allowable Raman transitions is $\Delta j = 0, \pm 2$. In a fashion similar to the case for vibrational scattering this selection rule arises from the orthogonality properties of the Legendre polynomials found in the eigenfunctions. To calculate the rotational selection rules it is necessary to know how the polarizability depends on the geometry between the molecule and the electric field. Figure 18 shows an arbitrarily oriented diatomic molecule in a linearly polarized electric field which is parallel to the z' axis. As a result of the orientation the induced polarization vector is not parallel to the electric field, and can be resolved into components perpendicular and parallel to the internuclear axis as shown. This results in $\mathbf{P} = \alpha_{xx}\mathbf{E}_x + \alpha_{zz}\mathbf{E}_z$. To obtain the net dipole moment caused by the electric field the projection of P onto the z' axis is taken. By trigonometry the result is $P_{z'} = [\alpha_{zz}\cos^2\theta + \alpha_{xx}\sin^2\theta]E_z$ from which the polarization can be taken, and with some manipulation written as

$$\alpha_{z'z'} = [\alpha_{zz} + (\alpha_{xx} - \alpha_{zz})\cos^2\theta] \qquad (C.10)$$

The resulting scattering matrix element has the form

$$P_{jj'} = \alpha_{zz}\int \psi_j^* \psi_{j'}\, d\mathrm{V} + (\alpha_{zz} - \alpha_{xx})\int \cos^2\theta \psi_j^* \psi_{j'}\, d\mathrm{V} \qquad (C.11)$$

The volume element dV denotes integration over all space in a spherical coordinate system. Because of the orthogonality properties of the Legendre polynomials the first integral is zero except for the case when $j = j'$ which, as in the vibrational case leads only to Rayleigh scattering and the selection rule $\Delta j = \pm 0$. Likewise the second integral is nonzero only for the case where $j - j' = \pm 2$ and gives the selection rule $\Delta j = \pm 2$. For H_2 the separation of rotational energy levels is on the order of hundredths of electron volts i.e. in the infrared. Such energy separations are typical of rotational Raman scattering, and of rotational spectroscopy in general.

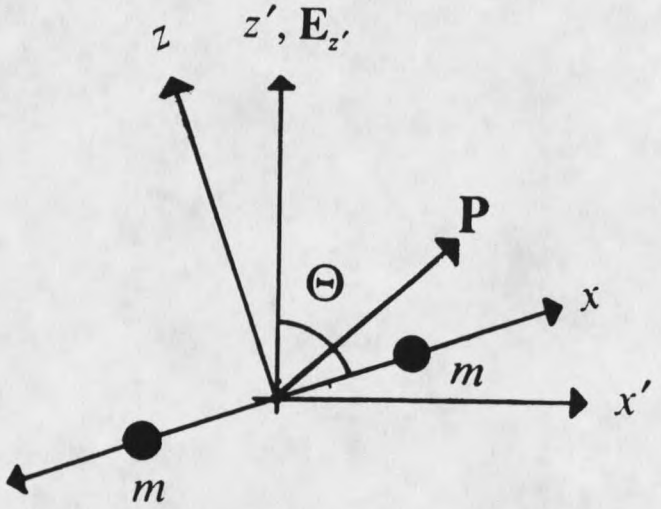


Figure 23. Geometry used in determining the form of the polarizability $\alpha_{z'z'}$ for rotational Raman scattering. The linearly polarized electric field is parallel to the z' axis. The polarizability is obtained by taking the projection of P onto the z' axis.

Of further interest is the fact that at room temperature the first excited rotational state is the most populated. This can be found by maximizing the Boltzmann distribution for the rotational state with respect to the quantum number j, that is

$$N_j \propto \frac{(I+1)}{I}(2j+1)e^{-E_j/k_BT} \qquad (C.12)$$

Here E_j is given by (C.8). The factor (I + 1)/I is due to nuclear degeneracy (related to the symmetry of the nuclear wave function) and equals 3 for rotational states of odd j values, and 1 for rotational states of even j values. For H_2 used in this work the degeneracy factor is 3. The (2j + 1) factor arises because of the degeneracy in the j^{th} level from the azimuthal quantum number m_j. When j is small the population increases due to the degeneracy term and the smallness of the exponential, however, when j becomes appreciable the exponential term dominates and drives the population down. Thus the population will have a maximum about some j value. Setting $dN_j/dj = 0$ and solving for maximum j leads to the result

$$j_{max} = \sqrt{\frac{Ik_BT}{\hbar^2}} - \frac{1}{2} \qquad (C.13)$$

Upon substitution of the appropriate values, this equation yields $j_{max} = 1$. Equation (C.13) shows that approximately 66 percent of the total population in the $j = 1$ state. Although the selection rule for rotational Raman scattering is $\Delta j = 0, \pm 2$ only the $\Delta j = 0$ case need be considered for this work. This is because linearly polarized light was used in the experiment, and is incapable of inducing any rotational excitation in the medium as it carries no intrinsic angular momentum[20]. As a result the $\Delta j = 0$ selection rule defines a so called "branch" in rotational spectroscopy and is denoted by Q. Specifically, the Raman scattering done in this thesis corresponds to $Q_{01}(1)$ with subscripted numbers denoting the initial and final vibrational levels, the number in parenthesis denoting the initial rotational

level, and Q denoting the selection rule $\Delta j = 0$. Additionally, the letters S, R, P, and O are used as nomenclature for the rotational spectroscopy selection rules of $\Delta j = +2, +1, -1, -2$ respectively[33].

Summary

In this appendix molecular hydrogen has been characterized as a Raman scattering medium through application of elementary spectroscopic theory. Among the more significant features discussed have been the fact that no electronic transitions are caused by the 308 nm pump photon, and that scattering is due to induced dipole moments for both vibrational and rotational scattering processes. Perhaps the most important results of this appendix are the selection rules for the various scattering processes. It was found that the vibrational selection rule is $\Delta v = -\pm 1$, and the rotational selection rule is $\Delta j = 0, \pm 2$. Additionally, it has been shown that vibrational Raman scattering is the primary scattering process in this work, while rotational scattering does not take place. This is attributed to the linearly polarized laser light which does not possess the angular momentum necessary to induce a rotational transition. The population of the vibrational and rotational levels was discussed, and it was found that at room temperature the ground vibrational and the first excited rotational states were most polulated. The branch defined by the selection rules and occupied states is denoted $Q_{01}(1)$.

MONTANA STATE UNIVERSITY LIBRARIES
3 1762 10109138 5